Petroleum Science 21 (2024) 3981–4000

Contents lists available at ScienceDirect

Petroleum Science

journal homepage: www.keaipublishing.com/en/journals/petroleum-science

Original Paper

Seismic data extrapolation based on multi-scale dynamic time warping

Jie-Li Li, Wei-Lin Huang *, Rui-Xiang Zhang

State Key Laboratory of Petroleum Resources and Prospecting, China University of Petroleum (Beijing), Beijing, 102249, China

ARTICLE INFO

Article history:
Received 26 December 2023
Received in revised form
11 May 2024
Accepted 12 June 2024
Available online 14 June 2024

Edited by Meng-Jiao Zhou

Keywords:
Seismic data reconstruction
Multi-scale morphology
Dynamic time warping
Extrapolation
Common-midpoint (CMP) gathers

ABSTRACT

Seismic data reconstruction can provide high-density sampling and regular input data for inversion and imaging, playing a crucial role in seismic data processing. In seismic data reconstruction, a common scenario involves a significant distance between the source and the first receiver, which makes it unattainable to acquire near-offset data. A new workflow for seismic data extrapolation is proposed to address this issue, which is based on a multi-scale dynamic time warping (MS-DTW) algorithm. MS-DTW can accurately calculate the time-shift between two time series and is a robust method for predicting time-offset ($t-x$) domain data. Using the time-shift calculated by the MS-DTW as the basic input, predict the two-way traveltime (TWT) of other traces based on the TWT of the reference trace. Perform autoregressive polynomial fitting on TWT and extrapolate TWT based on the fitted polynomial coefficients. Extract amplitude information from the TWT curve, fit the amplitude curve, and extrapolate the amplitude using polynomial coefficients. The proposed workflow does not necessitate data conversion to other domains and does not require prior knowledge of underground geological information. It applies to both isotropic and anisotropic media. The effectiveness of the workflow was verified through synthetic data and field data. The results show that compared with the method of predictive painting based on local slope, this approach can accurately predict missing near-offset seismic signals and demonstrates good robustness to noise.

© 2024 The Authors. Publishing services by Elsevier B.V. on behalf of KeAi Communications Co. Ltd. This is an open access article under the CC BY-NC-ND license (http://creativecommons.org/licenses/by-nc-nd/4.0/).

1. Introduction

At present, the description and exploration of oil and gas reservoirs are gradually developing towards high precision, high resolution, multi-scale, and deep layers (Liu et al., 2020; Zhou et al., 2023). Exploration targets are gradually shifting from areas with simple structures, shallow layers, and easy exploration and development to deep and complex geological areas with high exploration difficulty (Li and Qu, 2022; Zhou and Zhang, 2023). This development and transformation have put forward higher requirements for seismic data processing technology. Due to the complex underground geological conditions, the acquisition of field seismic data is often challenging to conduct in a consistent and regular manner (Huang, 2023). Sparse spatial sampling reduces the lateral resolution of underground profiles and affects imaging quality (Spitz, 1991). A common example of sparse spatial sampling occurs during ocean data acquisition, where there is a certain distance between the source and the first receiver, preventing the collection of near-offset data (Khoshnavaz, 2022). Almost all existing seismic data processing techniques require regular input data, otherwise it will seriously affect subsequent processing. Seismic data reconstruction technology can effectively regularize sparsely and irregularly sampled data. It can fill in missing seismic traces and provide high-density seismic data for high-precision inversion and imaging at a low cost (Lan et al., 2022; Huang, 2022; Hou et al., 2023).

The traditional methods for reconstructing seismic data can be divided into the following categories. The first type is based on wave equation methods (Li et al., 2023a), such as the joint reconstruction of missing seismic data using normal moveout (NMO) and inverse dip moveout (DMO) methods (Ronen, 1987), and the reconstruction of missing seismic data using azimuth moveout (AMO) local stacking method (Chemingui, 1996). This type of method is based on the velocity parameters of underground media, and utilizes iterative inversion of forward and inverse operators to

* Corresponding author.
E-mail addresses: cup_hwl@126.com, huangwl@cup.edu.cn (W.-L. Huang).

https://doi.org/10.1016/j.petsci.2024.06.009
1995-8226/© 2024 The Authors. Publishing services by Elsevier B.V. on behalf of KeAi Communications Co. Ltd. This is an open access article under the CC BY-NC-ND license (http://creativecommons.org/licenses/by-nc-nd/4.0/).

solve missing data. It has strong flexibility, but requires high accuracy in the underground velocity field. When the velocity information is not accurate enough, it affects the reconstruction effect and increases the computational workload. It is rarely applied in practical production. The second type of reconstruction method is based on predictive filtering (Fang et al., 2021; Liu et al., 2022b), which posits that plane waves are predictable in the frequency domain. This type of method utilizes the low-frequency components of the effective signal to derive prediction operators, thereby restoring the high-frequency components to be reconstructed. The predictive filtering operator is obtained by solving a least squares problem. This method has a strong anti-aliasing ability, but can only reconstruct regularly missing seismic data. The third type is based on compressive sensing methods (Bai et al., 2014; Zhang et al., 2017, 2021; Tang et al., 2020). This type of method posits that if a signal is sparse in a specific base space, it can be completely reconstructed even when the number of observed points is significantly lower than the Nyquist-Shannon sampling criterion (Orchard et al., 2012). By selecting appropriate mathematical functions to transform seismic data, sparse coefficients are processed within the transformation domain, and finally reconstructed data can be obtained through inverse transformation. The theory of compressive sensing aims to solve a least squares problem with 0/1 norm constraints. Commonly used methods for addressing this problem include the projections onto convex sets (POCS) method (Park et al., 2020; Oikawa et al., 2021; Chen et al., 2023) and the iterative shrinkage thresholding algorithm (ISTA) (Zheng et al., 2023; Li et al., 2023b). Due to the need to convert data to other domains, this type of method typically struggles to preserve the frequency and amplitude information of the original data well (Khoshnavaz et al., 2018; Khoshnavaz, 2022). Therefore, attenuation estimation of prestack seismic data is also an important research task for scholars (Liu et al., 2018, 2019). The fourth type is based on low-rank approximation methods (Sun et al., 2019; Cheng et al., 2019; Huang et al., 2020; Oboué and Chen, 2021). Consider clean and complete data as low-rank data. When the data structure is abnormal, it will increase the rank of seismic data. Therefore, the matrix can be reduced in rank to achieve seismic data reconstruction. This type of method is based on the assumption of linear events, and generally requires data partitioning. When the dimension of the rearranged Hankel matrix is large, the algorithm usually takes a long time and requires selecting the number of singular values for each data block (Cao et al., 2023). Due to the enormous amount of computation and data storage in practical applications, traditional seismic data reconstruction methods often suffer from problems such as prior constraints on reconstruction results, manual intervention required for hyperparameter selection, and low level of automation (Yi et al., 2023). So, researchers turned their attention to the rapidly developing field of deep learning. The basic principle is to obtain a nonlinear mapping function of the distribution characteristics of seismic data in the target block by learning a large number of seismic data samples, and then use the learned function to predict missing data. Representative deep learning seismic data reconstruction methods can be roughly divided into methods based on convolutional neural network (CNN) (Liu et al., 2021, 2022a; Chai et al., 2021; He et al., 2021), convolutional autoencoder (Wang et al., 2020; Song et al., 2020), recurrent neural network (RNN) (Yoon et al., 2021; Huangfu, 2021), and generative adversarial network (Creswell et al., 2018; Alwon, 2018). Data samples are a crucial factor that affects the effectiveness of deep learning seismic in data reconstruction. If the learned data features are too simplistic or if there is insufficient data used for training, serious generalization problems may arise during the reconstruction stage.

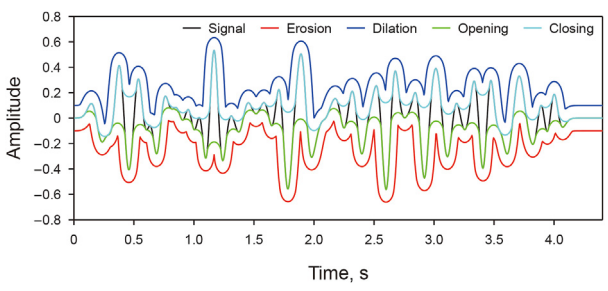

Fig. 1. The four fundamental operations of mathematical morphology.

Reconstructing seismic data in the time-offset ($t-x$) domain is the most fundamental and mainstream reconstruction technique. It does not require data conversion to other domains, thus better preserving the content of the original signal. Khoshnavaz (2022) utilized the predictive painting method (Fomel, 2010) to predict data within the $t-x$ domain. It is based on the local slope of seismic data and predicts each seismic trace by analyzing adjacent seismic traces. The local slope was obtained using plane-wave destruction (PWD) (Fomel, 2002). The accuracy of this method largely depends on the accuracy of local slope calculation. Due to its reliance on smoothing and regularization of seismic data, PWD has lower sensitivity to noise compared to other techniques. However, if the noise level is quite high, the accuracy of estimating the local slope using PWD will also be affected. The dynamic time warping (DTW) algorithm can directly establish the relationship between two time series, and can predict unknown seismic traces based on the relationship between known seismic traces. This algorithm was initially proposed in the field of speech recognition, utilizing dynamic programming to regularize time series (Vintsyuk, 1968). Smith and Waterman (1980) first introduced the DTW algorithm into geophysical research to calculate the correlation between strata. Later, this method developed rapidly and was widely applied in the field of seismic exploration. It includes horizon tracking of seismic data (Li and Liu, 2021; Li et al., 2021; Li and Huang, 2022), residual time difference correction (Luke and Zhang, 2019), time-shift estimation (Chen et al., 2018), seismic interferometry (Yuan et al., 2021), and similarity analysis (Kumar et al., 2022). The traditional DTW algorithm only matches the sequence point-to-point, ignoring the morphological connection between the signal and surrounding points, which makes the algorithm susceptible to noise. Seismic signals can be quantitatively described based on mathematical morphology due to their typical inclusion of information at different scales. Mathematical morphology originated in the field of image processing and was first applied in seismic data processing in 2005 (Wang et al., 2005). It has since developed widely and has become a powerful tool for seismic signal processing and analysis (Huang and Liu, 2020; Shang et al., 2022). In the traditional DTW algorithm, considering the relationship between signal forms can lead to a robust signal prediction algorithm called the multi-scale dynamic time warping (MS-DTW) algorithm (Li et al., 2023c).

This paper proposes a new workflow for seismic data reconstruction based on the MS-DTW algorithm. By directly correlating seismic traces with MS-DTW, we obtain time-shift information. Then, based on the time-shift, we extract the trend of seismic events and reconstruct the near-offset missing gathers in the common-midpoint (CMP) domain. This method has a simpler process, strong noise resistance, and high accuracy. The algorithm's performance was tested on synthetic data, and the result was accurate and reliable. Meanwhile, the superiority of this method was demonstrated by comparing it with the extrapolation method based on local slope proposed by Khoshnavaz (2022). Applying it to field data has verified the applicability of the method.

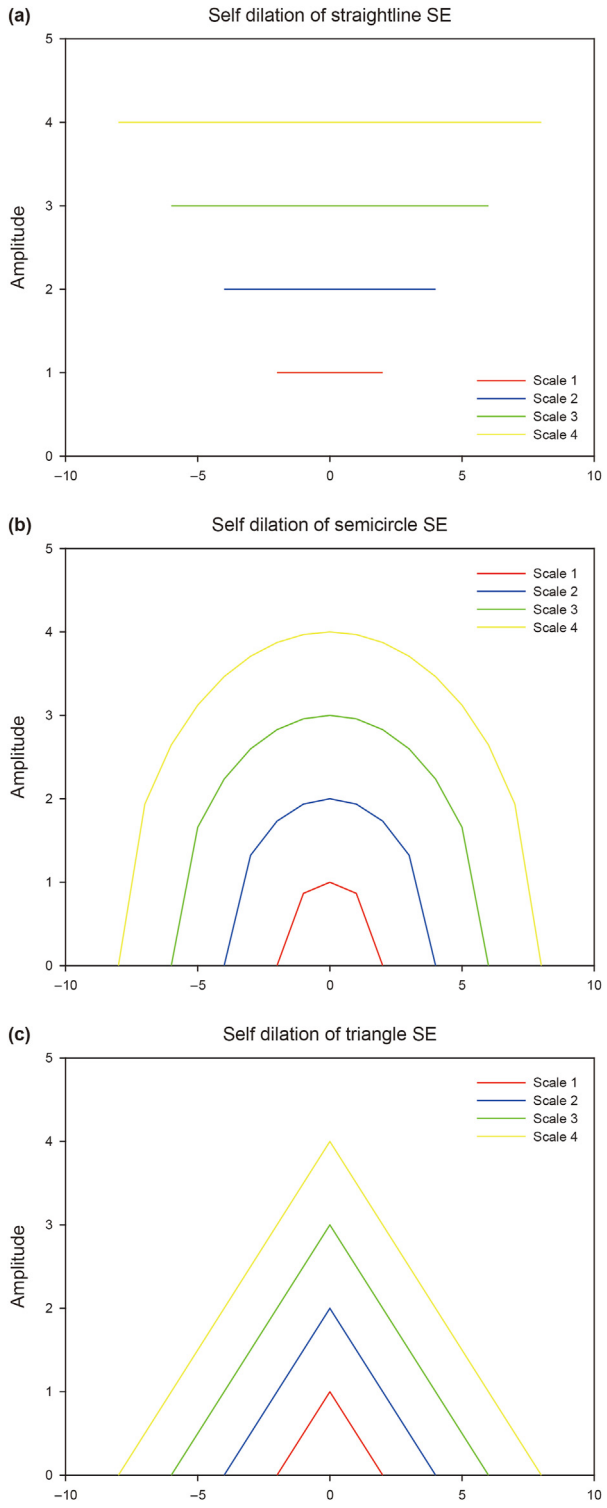

Fig. 2. SE group obtained through self-dilation. **(a)** Straightline SE, **(b)** semicircle SE, **(c)** triangle SE.

2. Methods

2.1. MS-DTW algorithm

As the name suggests, DTW is a dynamic programming algorithm that can automatically warp two time series by locally stretching or compressing the timeline to achieve the best match between them. The traditional DTW algorithm only matches the signal point-to-point, ignoring the relationship between the signal and surrounding points in amplitude changes. As a result, it cannot distinguish between noise signals and effective signals. When the data is contaminated by strong noise, the calculated time-shift results are inaccurate. Seismic records typically contain signals of various scales, reflecting different frequencies or durations, which can be quantitatively described using mathematical morphology. Introducing mathematical morphological information into traditional DTW not only matches signals point by point but also considers the variations in local signal morphology, leading to more accurate and robust signal matching.

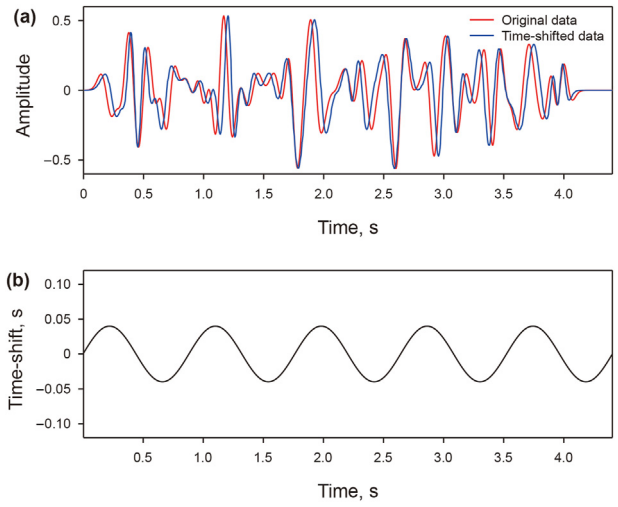

Fig. 3. **(a)** Original data (red line) and sinusoidal time-shifted data (blue line), **(b)** real time-shift curve.

In recent years, the exploration of mathematical morphology in the field of seismic exploration has been steadily increasing. The advantage of mathematical morphology lies in its ability to achieve various filtering purposes by changing structural elements (SE). This significantly broadens the application scope of mathematical morphology in the field of seismic exploration. Mathematical morphological filtering is based on stochastic integral geometry theory and logical topology theory, and can be seen as the mutual operation of two datasets. In seismic signal processing, one dataset typically consists of the seismic time series $\boldsymbol{t} = [t(i)]$ that requires processing, while the other dataset is the SE $\boldsymbol{b} = [b(\tau)]$. Mathematical morphological filtering involves four basic operators: dilation, erosion, opening, and closing. Among them, dilation and erosion are the most fundamental operators. The dilation $\oplus$ and erosion $\ominus$ operations performed on $t(i)$ using $b(\tau)$ are defined as (Huang et al., 2018)

$$\boldsymbol{t} \oplus \boldsymbol{b} = \max_{\tau}\{t(i-\tau) + b(\tau)\} \tag{1}$$

$$\boldsymbol{t} \ominus \boldsymbol{b} = \min_{\tau}\{t(i+\tau) - b(\tau)\} \tag{2}$$

Opening $\circ$ and closing $\cdot$ are completed by a combination of dilation and erosion operations, respectively defined as

$$\boldsymbol{t} \circ \boldsymbol{b} = (\boldsymbol{t} \ominus \boldsymbol{b}) \oplus \boldsymbol{b} \tag{3}$$

$$\boldsymbol{t} \cdot \boldsymbol{b} = (\boldsymbol{t} \oplus \boldsymbol{b}) \ominus \boldsymbol{b} \tag{4}$$

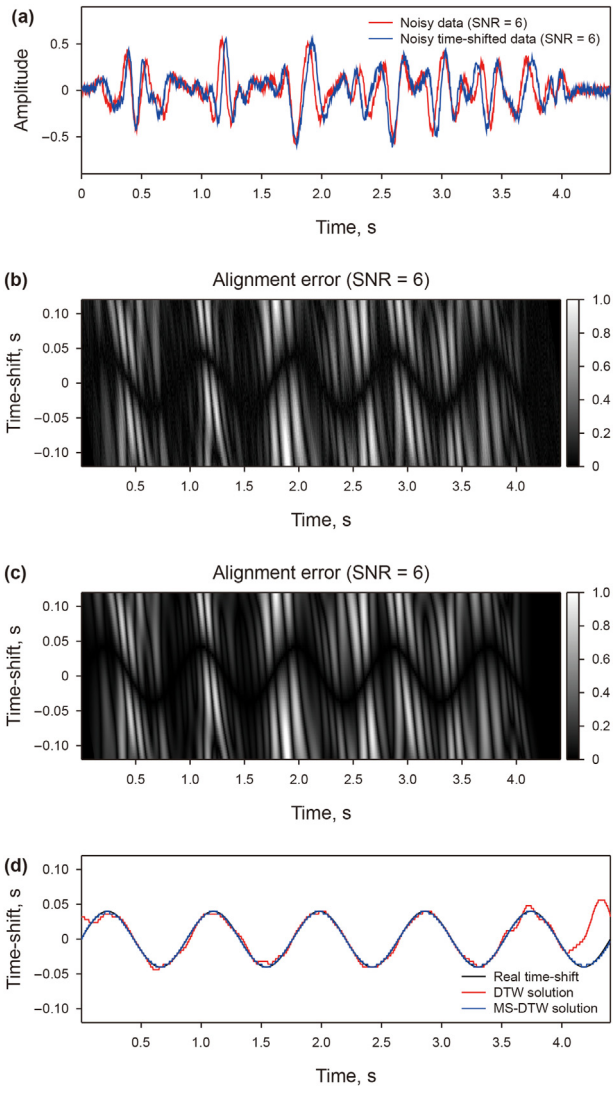

Fig. 4. **(a)** Noisy data (red line) and noisy time-shifted data (blue line) with a SNR of 6, **(b)** alignment error obtained by traditional DTW algorithm, **(c)** alignment error obtained by MS-DTW algorithm, **(d)** real time-shift curve (black line) and time-shift curve calculated by traditional DTW (red line) and MS-DTW (blue line) respectively.

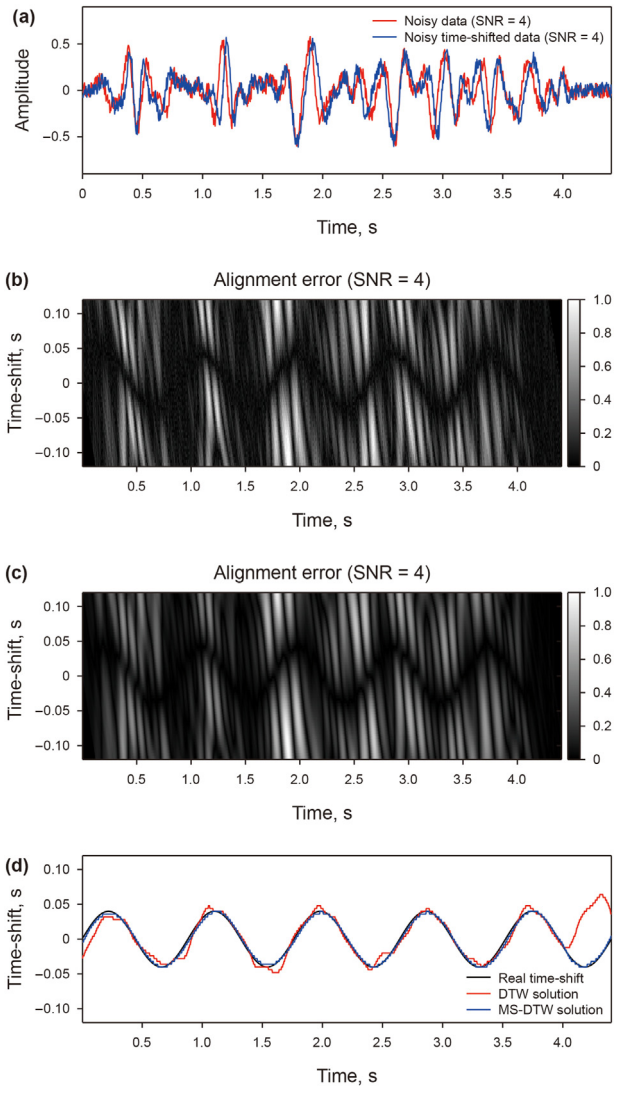

Fig. 5. **(a)** Noisy data (red line) and noisy time-shifted data (blue line) with a SNR of 4, **(b)** alignment error obtained by traditional DTW algorithm, **(c)** alignment error obtained by MS-DTW algorithm, **(d)** real time-shift curve (black line) and time-shift curve calculated by traditional DTW (red line) and MS-DTW (blue line) respectively.

Fig. 1 illustrates the four fundamental operations of mathematical morphology using semicircle SE. The black line represents the original signal, while the red, blue, green, and cyan lines represent erosion, dilation, opening, and closing operations, respectively.

Traditional morphological filtering is the arithmetic mean of alternating opening and closing operations:

$$f_b(t) = [(\boldsymbol{t} \circ \boldsymbol{b}) \cdot \boldsymbol{b} + (\boldsymbol{t} \cdot \boldsymbol{b}) \circ \boldsymbol{b}] / 2 \tag{5}$$

where f_b represents the mathematical morphological filtering of SE $\boldsymbol{b}$ on signal $\boldsymbol{t}$. It can be seen that the performance of morphological filtering is determined by the shape of SE. For seismic exploration, SE is often an axisymmetric nonconcave function, with commonly used shapes including straightline, semicircle, and triangle. The selection of SE shape is related to the input signal and processing target. For example, the straightline SE can be used for seismic coherent noise suppression by sliding it along the trajectory of the coherent noise. Semicircle SE usually detects the morphological information of the signal along the time direction of each seismic trace, as its shape can better match the seismic waveform compared to straightline SE (Huang et al., 2018). Therefore, the semicircle SE was utilized in this study. So far, triangle SE has been rarely used in seismic data processing, but it is widely utilized in image processing, such as corner detection (Sobania and Evans, 2005).

In the process of applying mathematical morphology filtering, a single SE often cannot effectively represent all the features of the signal. To solve this problem, a multi-scale mathematical morphology method has been proposed, which uses SE of different scales to perform mathematical morphology filtering on the signal. Typically, a set of SE can be generated using the self-dilation method. Fig. 2(a)–(c) show the sets of straightline, semicircle, and triangle SE, respectively.

Given a set of SE $\boldsymbol{b}_k$ with different morphological scales, $k \in [1,K]$, where k represents the morphological scale. A certain signal $\boldsymbol{t}$ can be represented as the sum of $K+1$ components:

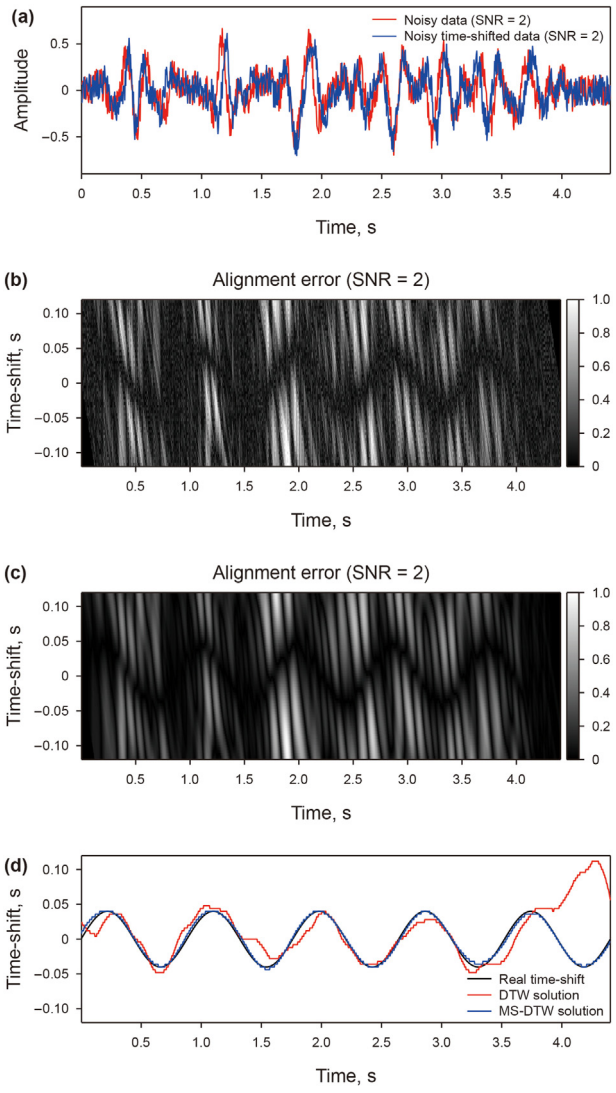

Fig. 6. **(a)** Noisy data (red line) and noisy time-shifted data (blue line) with a SNR of 2, **(b)** alignment error obtained by traditional DTW algorithm, **(c)** alignment error obtained by MS-DTW algorithm, **(d)** real time-shift curve (black line) and time-shift curve calculated by traditional DTW (red line) and MS-DTW (blue line) respectively.

$$\begin{aligned}\boldsymbol{t} &= f_{b_0}(\boldsymbol{t}) - f_{b_1}f_{b_0}(\boldsymbol{t}) + f_{b_1}f_{b_0}(\boldsymbol{t}) \\ &= f_{b_0}(\boldsymbol{t}) - f_{b_1}f_{b_0}(\boldsymbol{t}) + f_{b_1}f_{b_0}(\boldsymbol{t}) - f_{b_2}f_{b_1}f_{b_0}(\boldsymbol{t}) + f_{b_2}f_{b_1}f_{b_0}(\boldsymbol{t}) \\ &\cdots \\ &= \sum_{k=1}^{K}\left[f_{b_{k-1}}\cdots f_{b_1}f_{b_0}(\boldsymbol{t}) - f_{b_k}\cdots f_{b_1}f_{b_0}(\boldsymbol{t})\right] + f_{b_k}\cdots f_{b_1}f_{b_0}(\boldsymbol{t})\end{aligned} \tag{6}$$

where $f_{b_0}(\boldsymbol{t}) = \boldsymbol{t}$. The above equation is called multi-scale morphological decomposition. Essentially, it is a series of morphological filters with different scales applied to a certain signal. For convenience, let

$$\boldsymbol{c}_k = \begin{cases} f_{b_{k-1}}\cdots f_{b_1}f_{b_0}(\boldsymbol{t}) - f_{b_k}\cdots f_{b_1}f_{b_0}(\boldsymbol{t}) \ , \ k\in[1,K] \\ f_{b_k}\cdots f_{b_1}f_{b_0}(\boldsymbol{t}), k = K+1 \end{cases} \tag{7}$$

where $\boldsymbol{c}_k$ is a multi-scale component, $k\in[1,K+1]$. For two seismic signals $\boldsymbol{p}$ and $\boldsymbol{q}$ with length n, given the SE group $\boldsymbol{b}_k$, they can be decomposed into

$$\boldsymbol{p} = \boldsymbol{P}[\boldsymbol{p}_1, \boldsymbol{p}_2, \ldots, \boldsymbol{p}_K, \boldsymbol{p}_{K+1}] \tag{8}$$

$$\boldsymbol{q} = \boldsymbol{Q}[\boldsymbol{q}_1, \boldsymbol{q}_2, \ldots, \boldsymbol{q}_K, \boldsymbol{q}_{K+1}] \tag{9}$$

Calculate the alignment error $\boldsymbol{e}_k$ of two sequences separately at the same morphological scale. When the alignment error is zero, it indicates that the two signals are completely aligned. The alignment error at the kth scale can be expressed as

$$e_k[i, l[i]] \equiv (p_k[i] - q_k[i + l[i]])^2 \tag{10}$$

where $l[i]$ represents the time-shift of the ith sampling point in seismic signal $\boldsymbol{q}$, and let $l[i]$ be an integer from $-L$ to L, with a length of $2L+1$. From this, a set of alignment errors $\boldsymbol{E}[\boldsymbol{e}_1, \boldsymbol{e}_2, \ldots, \boldsymbol{e}_K, \boldsymbol{e}_{K+1}]$ with different morphological scales can be obtained. By giving $K+1$ weight factors $\boldsymbol{W}[w_1, w_2, \ldots, w_K, w_{K+1}]$, the final alignment error can be expressed as:

$$\boldsymbol{e} = \sum_{k=1}^{k=K+1} w_k \boldsymbol{e}_k \tag{11}$$

where weight coefficient $w_k \in \{0, 1\}$ (Li et al., 2023c). Based on alignment error, the following constraint minimization problem can be solved to obtain the time-shift sequence $\Delta\boldsymbol{t}$ of two seismic signals:

$$\Delta\boldsymbol{t} = \underset{l}{\operatorname{argmin}} \sum_{i=0}^{n-1} \boldsymbol{e} \tag{12}$$

The above constraint minimization problem can be solved using the concept of dynamic programming. Firstly, the problem is decomposed into a series of subproblems, which are processed to obtain the final solution of the algorithm. Specifically, it can be achieved through two steps: accumulation and backtracking (Venstad, 2014; Hale, 2013; Chen et al., 2018), which have been described in detail by many researchers. Therefore, we will not discuss them further here.

To test the performance of the MS-DTW algorithm mentioned above, we generated a seismic record by convolving random reflection coefficients with Ricker wavelet, as illustrated by the red line in Fig. 3(a). The blue line in Fig. 3(a) represents the seismic record after sinusoidal time-shift of the red line. The time-shift is depicted in Fig. 3(b). To analyze the impact of different noise intensities on the accuracy of the time-shift curve, we added random noise with signal-to-noise ratio (SNR) of 6, 4, and 2 to the seismic records mentioned above. The results are shown in Figs. 4(a), 5(a) and 6(a), respectively. Taking the signal with a SNR of 6 as an example to illustrate the results of multi-scale filtering, as shown in Fig. 7. Here, we use six semicircle SE to process noisy signals. Fig. 7(a) shows the multi-scale filtering results of the noisy seismic record before time-shift. As the morphological scale increases, it can be observed that the signal tends to become smoother. Therefore, the influence of random noise can be suppressed by assigning smaller weights to small-scale signals. Fig. 7(b) shows the results of multi-scale filtering of the noisy seismic record after time-shift. Compared with Fig. 7(a), it can be seen that signals at the same scale have similar shapes. To emphasize the superiority of the MS-DTW algorithm, we compare it with the traditional DTW algorithm. The alignment errors calculated using the traditional DTW algorithm are shown in Figs. 4(b), 5(b) and 6(b), respectively, while the alignment errors calculated using the MS-DTW algorithm are shown in Figs. 4(c), 5(c) and 6(c), respectively. By comparison, it can be seen that the sinusoidal black trajectory in the alignment error obtained by the MS-DTW algorithm is more pronounced. The time-shift curves calculated for different noise intensities are shown in

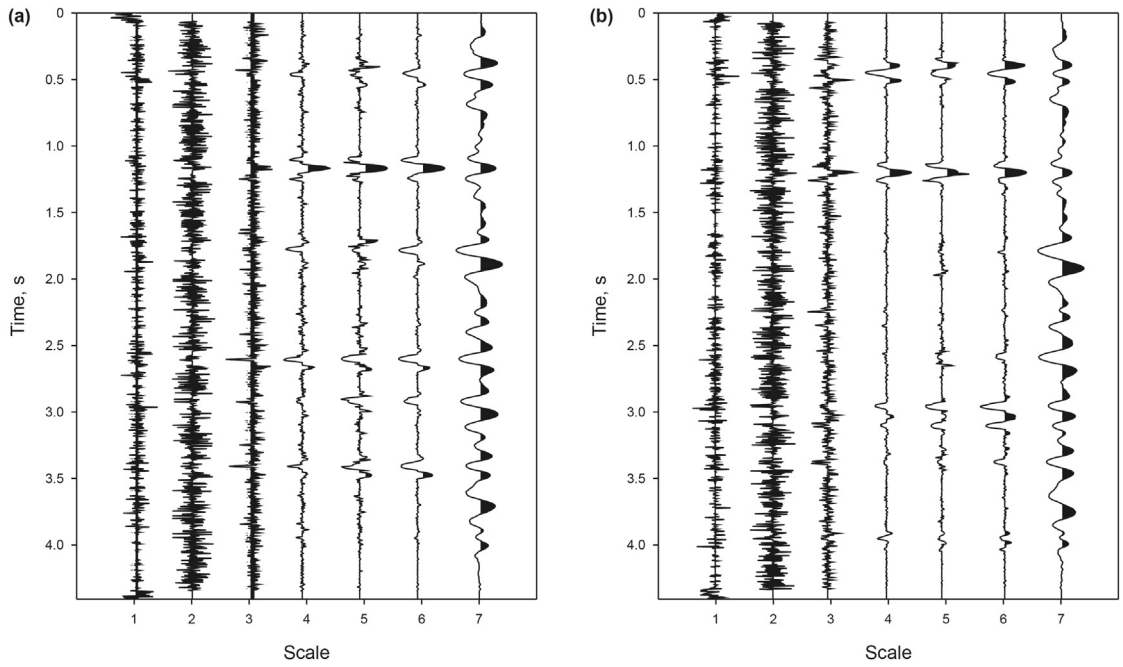

Fig. 7. **(a)** Multi-scale decomposition of the noisy original seismic record with a SNR of 6 using six semicircle SE, **(b)** multi-scale decomposition of the noisy time-shifted seismic record with a SNR of 6 using six semicircle SE.

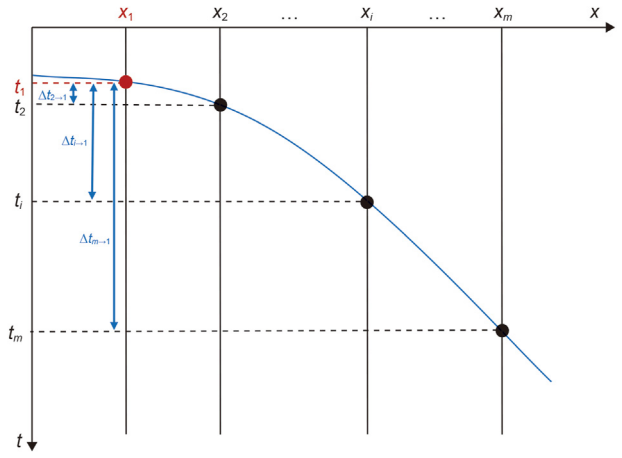

Fig. 8. Calculate TWT based on time-shift.

Figs. 4(d), 5(d) and 6(d), respectively. The black line represents the real time-shift curve, the red line represents the time-shift curve calculated by the traditional DTW algorithm, and the blue line represents the time-shift curve calculated by the MS-DTW algorithm. It can be seen that as the noise intensity increases, the traditional DTW algorithm exhibits significant local fluctuations and is highly sensitive to noise. However, the time-shift obtained by the MS-DTW algorithm consistently matches well with the real time-shift, indicating that the method is not sensitive to noise.

2.2. Seismic data extrapolation

The missing seismic profile to be processed is represented as $\boldsymbol{X} = [\boldsymbol{x}_1, \boldsymbol{x}_2, \ldots, \boldsymbol{x}_i, \ldots, \boldsymbol{x}_m]$, consisting of m seismic traces, with an increasing offset from the first to the mth trace. Select one of the traces as the reference trace and utilize the MS-DTW algorithm to calculate the time-shift between the other traces and the reference trace. The time-shift $\Delta\boldsymbol{t}_{i\to\text{refer}}$ between the ith trace and the reference trace can be expressed as

$$\Delta\boldsymbol{t}_{i\to\text{refer}} = MSDTW\left(\boldsymbol{x}_{\text{refer}}, \boldsymbol{x}_i\right) \tag{13}$$

where $MSDTW(\cdot)$ represents the MS-DTW operation introduced in the previous section. For a certain seismic event/wavefront, the reference seismic trace's sample point coordinate at that seismic event is $(x_{\text{refer}}, t_{\text{refer}})$. By calculating the time-shift between other traces and the reference trace, it can be used as the basic input for seismic data extrapolation workflow to predict the two-way traveltime (TWT) of other traces. Among them, the TWT of the ith trace can be expressed as

$$t_i = t_{\text{refer}} + \Delta t_{i\to\text{refer}}, i \in [1, m] \tag{14}$$

Fig. 8 illustrates an ideal seismic event in the CMP gather without wavelet effects. Here, we select the first trace as the reference trace, and the reference point is the red point in the figure, with coordinates (x_1, t_1). It can be seen that the TWT of other traces is related to the TWT of the reference trace as follows:

$$t_2 = t_1 + \Delta t_{2\to1} \tag{15}$$

$$t_i = t_1 + \Delta t_{i\to1} \tag{16}$$

$$t_m = t_1 + \Delta t_{m\to1} \tag{17}$$

We use the individual seismic event in Fig. 9 as an example to illustrate the basic process of seismic data extrapolation. This event has 25 seismic traces. Assuming the first five traces are missing, predict them based on the latter part of the data. The reference trace is the first trace, which is the trace where the red point is located in Fig. 9(a). The TWT of the red point corresponds to the peak of the trace. Using the MS-DTW algorithm to calculate the time-shift of other traces relative to the trace where the red point is located, and to determine the TWT of other seismic traces, as

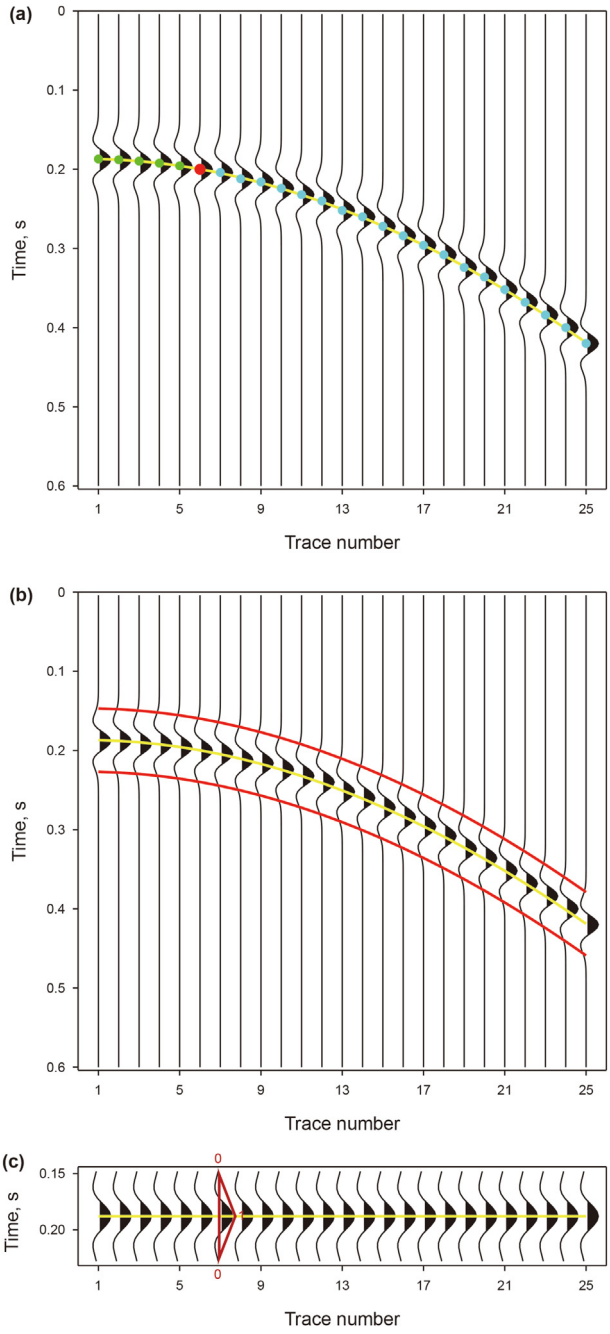

Fig. 9. **(a)** TWT extrapolation diagram, **(b)** extract time window based on TWT, **(c)** weighted extrapolation of amplitude within the flattened time window.

shown in the cyan point in Fig. 9(a), it can be observed that the TWTs of the cyan points also align with the peak of the trace where they are located. According to the coordinates of the red and cyan points, autoregressive polynomial fitting can be performed to obtain a TWT curve, as depicted by the yellow line in Fig. 9(a). Use the obtained polynomial coefficients to extrapolate the TWT, and the green points represent the TWT obtained from the extrapolation, which also corresponds well to the position of the wave peak. Of course, we need to understand that the selection of the reference trace is not unique. In theory, any seismic trace that is not missing can be used as a reference trace. However, traces with smaller offsets typically contain more accurate information, making them more conducive to the workflow. Therefore, selecting the first trace

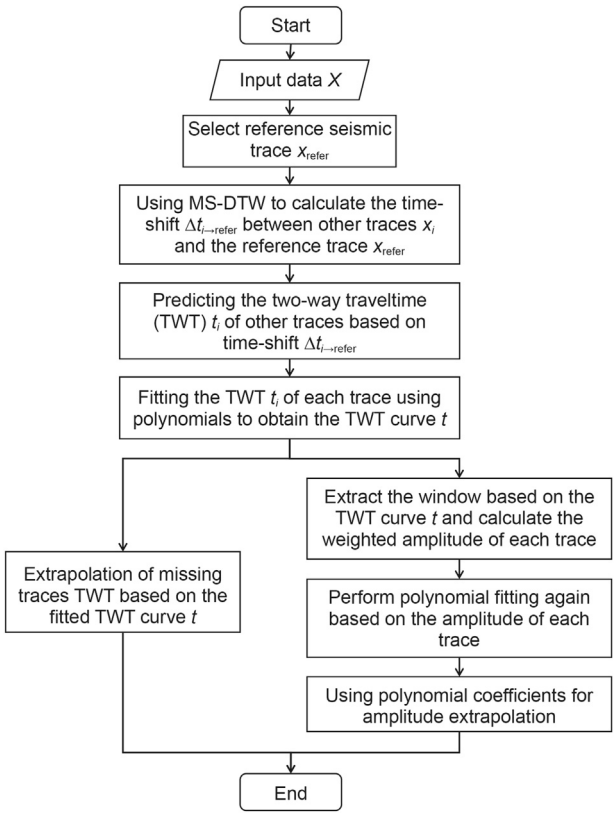

Fig. 10. Seismic data extrapolation flowchart.

that is not missing is always a good choice.

Next, predict the amplitude information on the TWT curve. To improve the accuracy of prediction, we use the predicted TWT curve as the center and select a window. The red line in Fig. 9(b) represents the selected window boundary. Extracting this window can obtain a flattened seismic event, as depicted in Fig. 9(c). A weighted sum is performed on the amplitude values of each seismic trace within the window. To emphasize the amplitude located on the TWT curve, a trigonometric operator is used as the weight, as indicated by the red triangle in Fig. 9(c). Given the amplitude weight on the TWT curve as 1, the weight gradually decreases towards both sides of the window. Extract the amplitude information of each trace based on the TWT curve, perform autoregressive polynomial fitting on the amplitudes, and utilize the resulting polynomial coefficients for amplitude extrapolation. Fig. 10 summarizes the workflow of the seismic data extrapolation method based on MS-DTW.

3. Synthetic data example

The synthetic data is used to test the performance of the proposed extrapolation workflow. Fig. 11(a) shows the data generated by inverse NMO using linearly changing velocity over time. The time sampling interval is 4 ms, and the spatial sampling interval is 20 m, including 17 seismic events. We muted 20% of the near offset seismic traces and the result is shown in Fig. 11(b). Random noise with SNR of 6, 4, and 2 was separately added to the muted data to test the performance of the proposed workflow. The noisy data are shown in Fig. 12(a)–(c), respectively. At the same time, a comparative analysis was conducted between the proposed method and the method proposed by Khoshnavaz (2022). Khoshnavaz used PWD (Fomel, 2002) to calculate the local slope. Subsequently, based

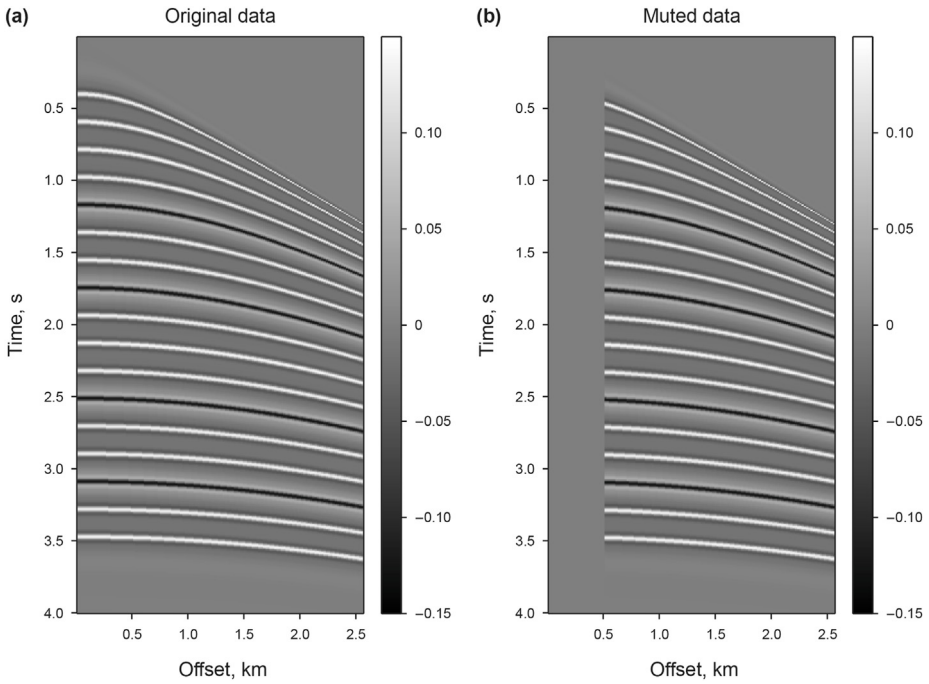

Fig. 11. **(a)** Original synthetic data, **(b)** synthetic data after muted 20%.

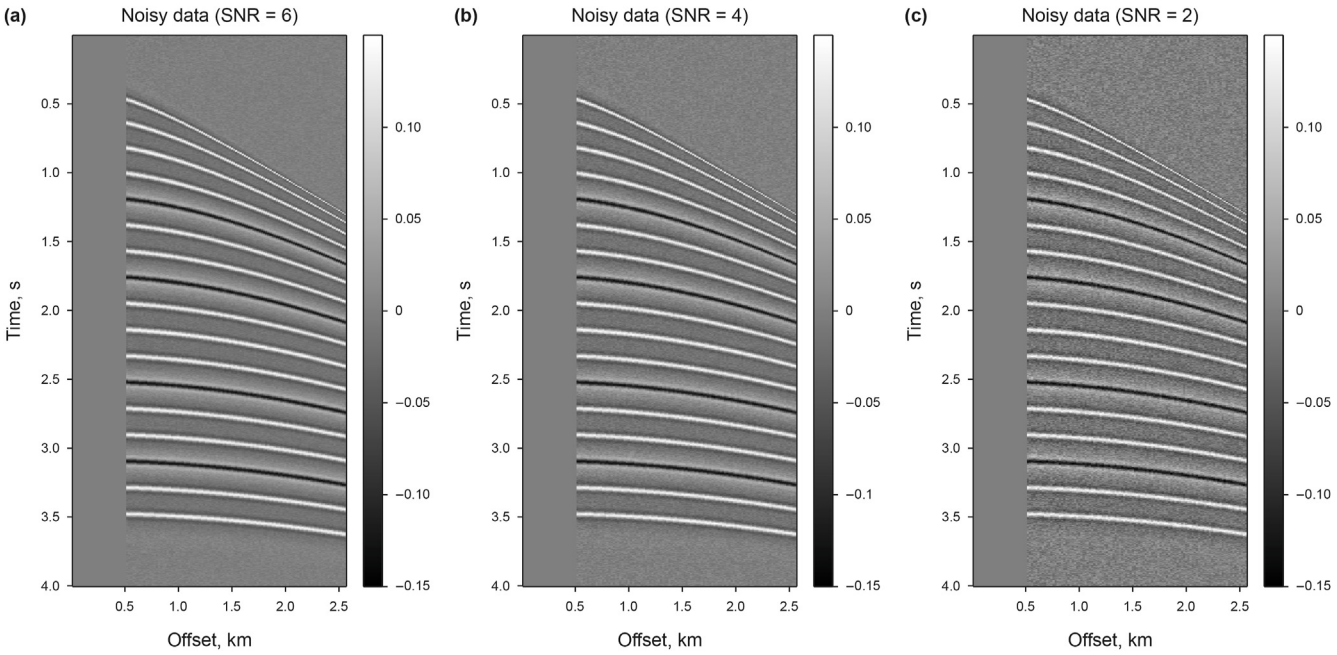

Fig. 12. **(a)** Noisy synthetic data (SNR = 6) after muted 20%, **(b)** noisy synthetic data (SNR = 4) after muted 20%, **(c)** noisy synthetic data (SNR = 2) after muted 20%.

on the local slope, predictive painting (Fomel, 2010) was used to obtain TWT, and flattened to display the TWT-warping profile. Fig. 13(a) shows the TWT-warping profile of noisy data obtained using the method proposed by Khoshnavaz (2022) when the SNR is 6. It can be seen that the continuity of this profile in the temporal direction is poor. The extrapolated TWT-warping profile is shown in Fig. 13(b). Based on the TWT-warping profile, the data with a SNR of 6 was extrapolated, and the results are shown in Fig. 14(a). The shallow extrapolation results are not ideal. Meanwhile, in Fig. 14(b), we present the residual profile between the extrapolated data and the original noisy data. There are many seismic events in the residual profile, with shallow seismic events being more pronounced. To quantify the accuracy of the results, we calculated the relative error of the amplitude residual of the missing seismic traces relative to the original amplitude of the region, which is 34.87%, indicating a significant error.

Next, we use the proposed workflow to extrapolate the synthetic data with a SNR of 6. When using the MS-DTW algorithm, we used five semicircle SE and selected the first unmute seismic trace as the reference trace to estimate the time-shift of the data. The

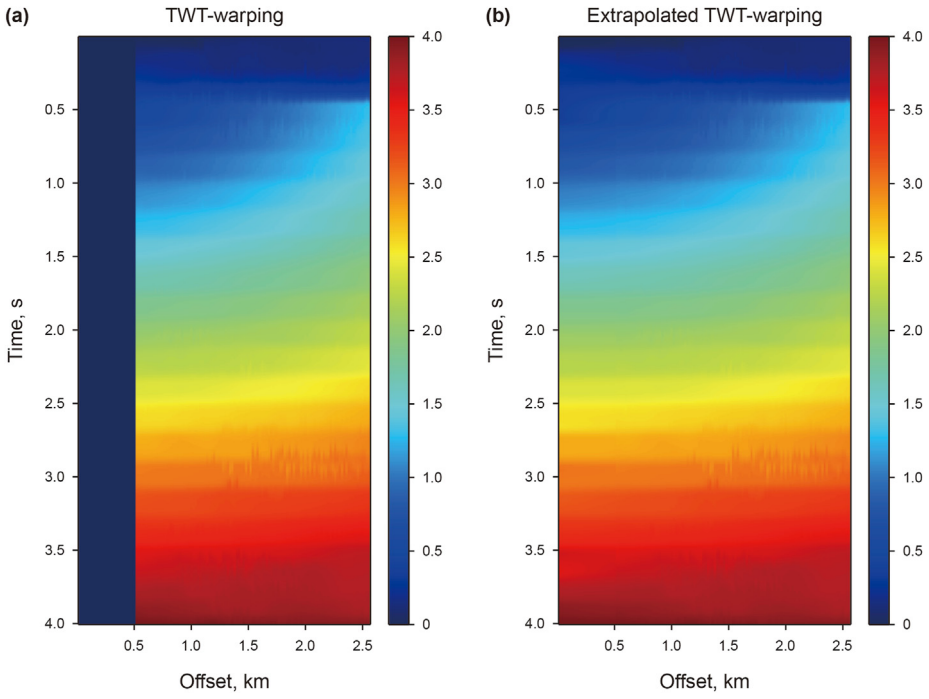

Fig. 13. **(a)** TWT-warping profile of noisy data with a SNR of 6 obtained through predictive painting, **(b)** extrapolated TWT-warping profile.

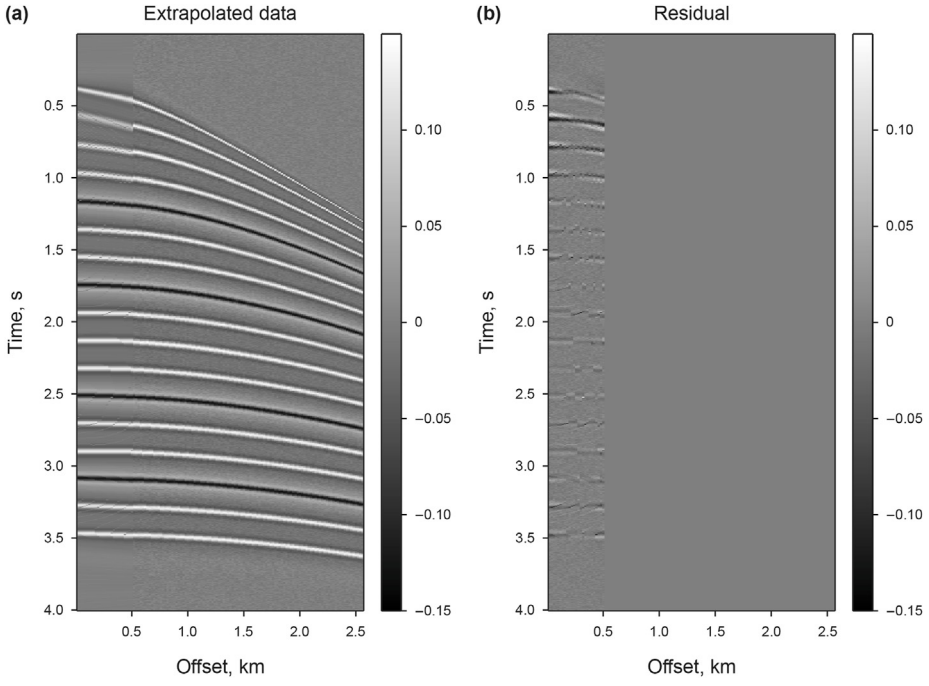

Fig. 14. **(a)** Extrapolated data through Khoshnavaz (2022) method (SNR = 6), **(b)** the residual between the extrapolated data and noisy data with a SNR of 6.

results are shown in Fig. 15(a). Overall, the time-shift gradually increases with the increase of offset, and in the temporal direction, it gradually decreases, which is consistent with the synthetic data we constructed. However, in the horizontal direction, the time-shift is only continuous in some places, and these times correspond to the zero offset TWT of the seismic event. This is because the amplitude energy corresponding to the seismic event is strong and shows regularity, while the position without the event is disordered due to the randomness of the noise, meaning it is discontinuous in the horizontal direction. We use time-shift as the basic input, calculate the TWT of each trace according to Eq. (14), flatten the TWT profile and display it, as shown in Fig. 15(b). Autoregressive polynomial fitting was performed on each TWT, utilizing fourth-order polynomial fitting. The TWT curves were extrapolated based on the fitted polynomial coefficients, and the extrapolation results are depicted in Fig. 15(c). By extracting

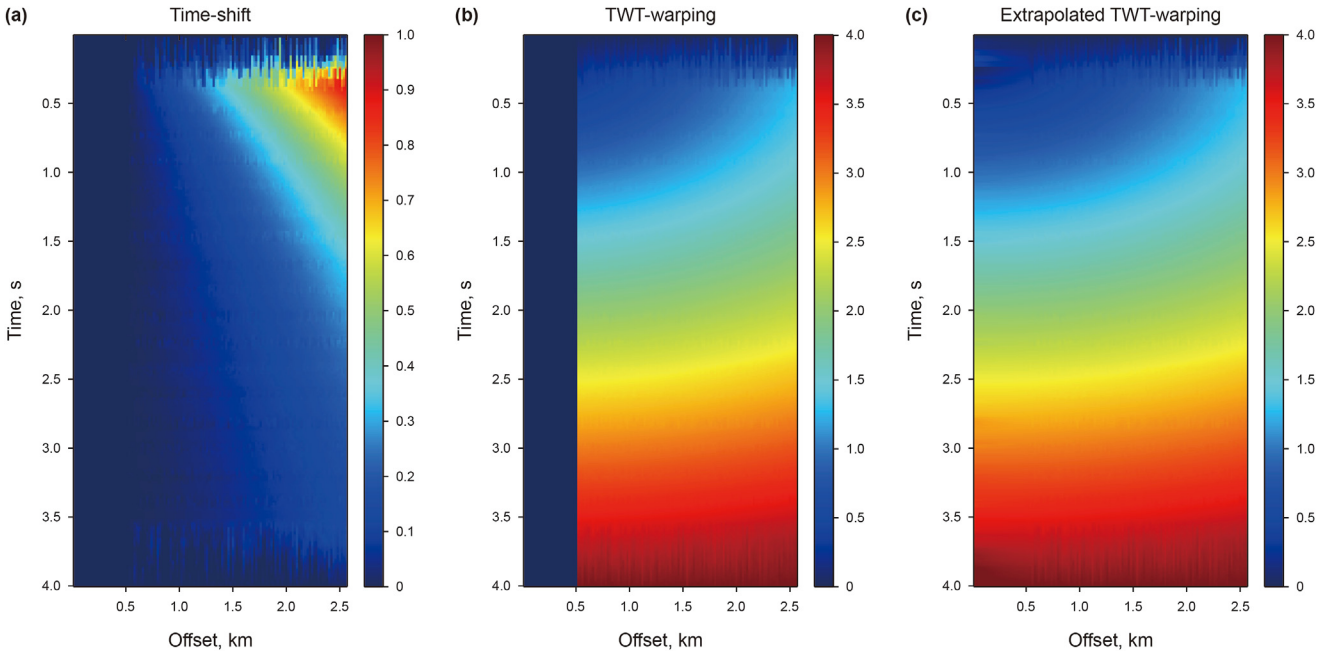

Fig. 15. **(a)** Time-shift of noisy data with SNR 6 calculated by MS-DTW, **(b)** TWT-warping profile calculated based on time-shift, **(c)** extrapolated TWT-warping profile.

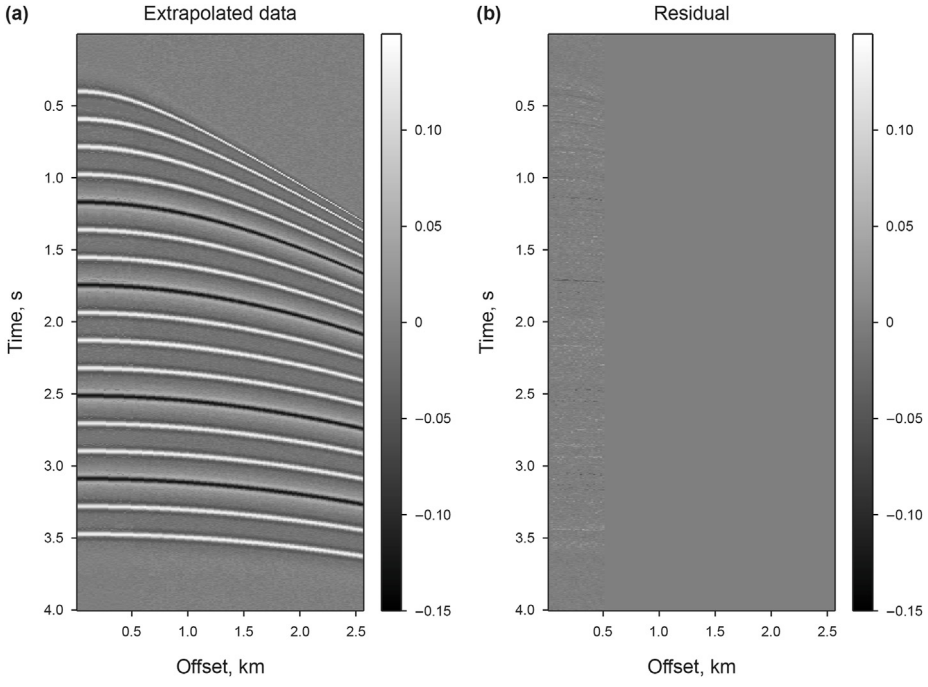

Fig. 16. **(a)** Extrapolated data using the proposed workflow (SNR = 6), **(b)** the residual between the extrapolated data and noisy data with a SNR of 6.

amplitude information from TWTs and performing polynomial fitting on the weighted amplitudes, the corresponding amplitude trend can be obtained, thus completing the complete extrapolation workflow. Fig. 16(a) shows the extrapolated results of the near-offset seismic traces, and we also display the residual values between the extrapolated data and the original noisy data, as shown in Fig. 16(b). It can be seen that the seismic events in the residual profile are not significant. To quantify the accuracy of the proposed workflow, we calculated the average relative error of the reconstructed data amplitude, which is 21.90%. Compared with the method proposed by Khoshnavaz (2022), this error is significantly reduced.

We use the same steps to test data with a SNR of 4. Fig. 17(a), (b) respectively show the TWT-warping profile and their extrapolation profile obtained by Khoshnavaz (2022) method. It can be seen that as the noise intensity increases, the predicted TWT becomes more discontinuous in the temporal direction. Based on Fig. 17(b), extrapolated seismic data was obtained, as shown in Fig. 18(a). Due to the influence of noise, the deep extrapolation results also become inaccurate. Fig. 18(b) shows the residual values between

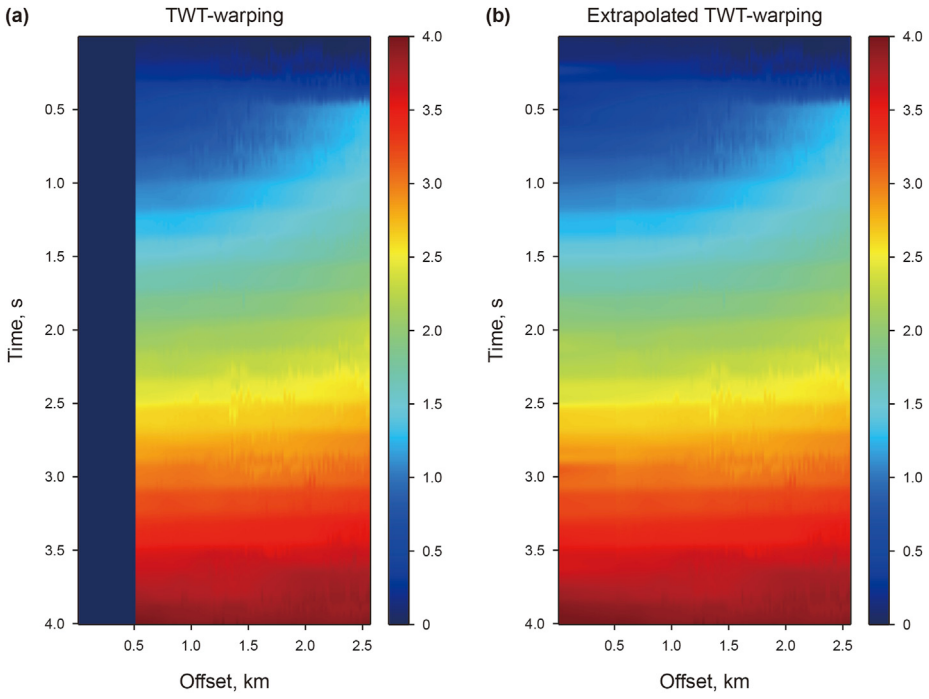

Fig. 17. **(a)** TWT-warping profile of noisy data with a SNR of 4 obtained through predictive painting, **(b)** extrapolated TWT-warping profile.

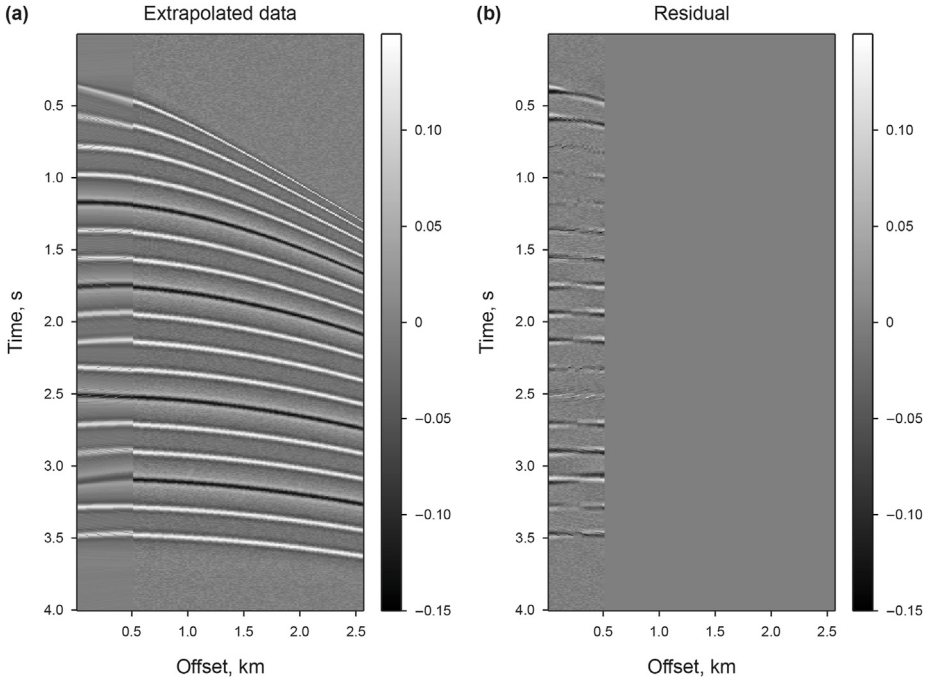

Fig. 18. **(a)** Extrapolated data through Khoshnavaz (2022) method (SNR = 4), **(b)** the residual between the extrapolated data and noisy data with a SNR of 4.

the extrapolated data and the original noisy data, where seismic events are evident. The average relative error of amplitude in the reconstructed part is 54.68%. The time-shift, TWT-warping profile, and its extrapolation profile calculated using the proposed workflow are shown in Fig. 19(a)–(c), respectively. The reconstructed data and residual profile are shown in Fig. 20(a) and (b), respectively, with very few residual seismic events in the residual profile. The average relative error of the amplitude reconstructed from this data is 30.48%. Compared with the Khoshnavaz (2022) method, the reconstruction accuracy has significantly improved, leading to a decrease in errors. Figs. 21 and 22 show the processing results of the method proposed by Khoshnavaz on data with a SNR of 2. Due to the influence of strong noise, the performance of this method further decreases, with a large number of seismic events remaining in the residual profile. The average relative error of the amplitude reconstructed from this data is 77.56%, indicating very poor

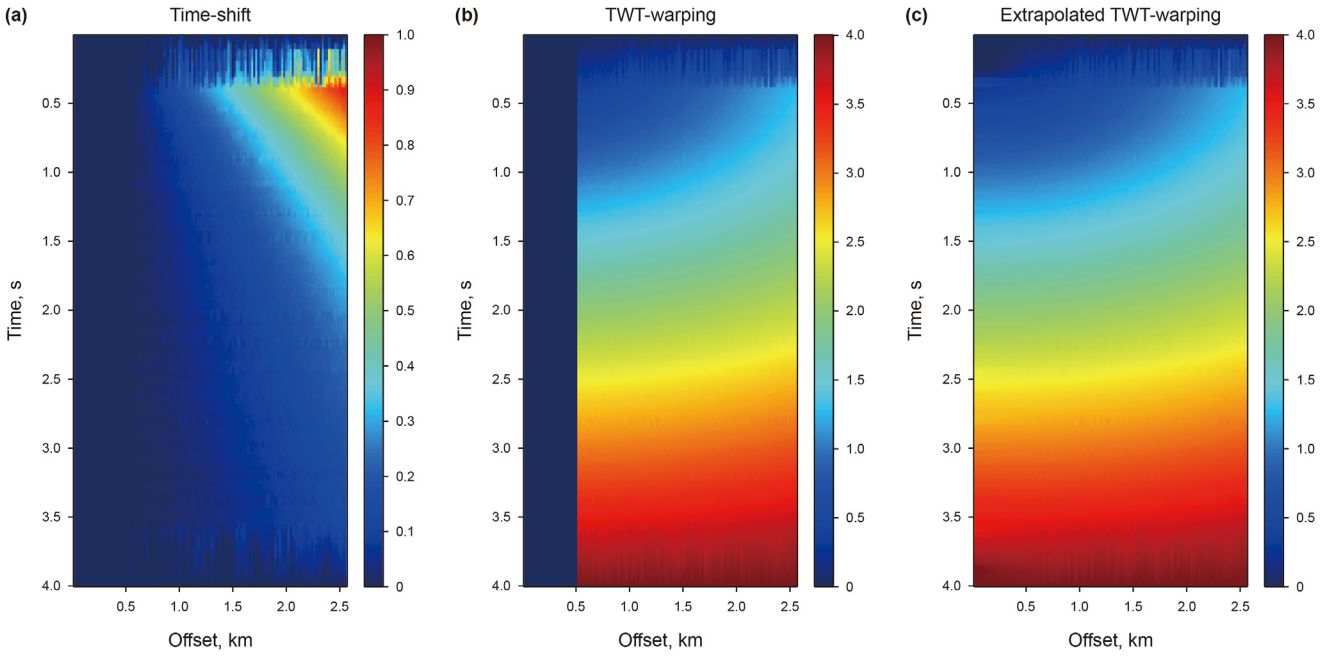

Fig. 19. **(a)** Time-shift of noisy data with SNR 4 calculated by MS-DTW, **(b)** TWT-warping profile calculated based on time-shift, **(c)** extrapolated TWT-warping profile.

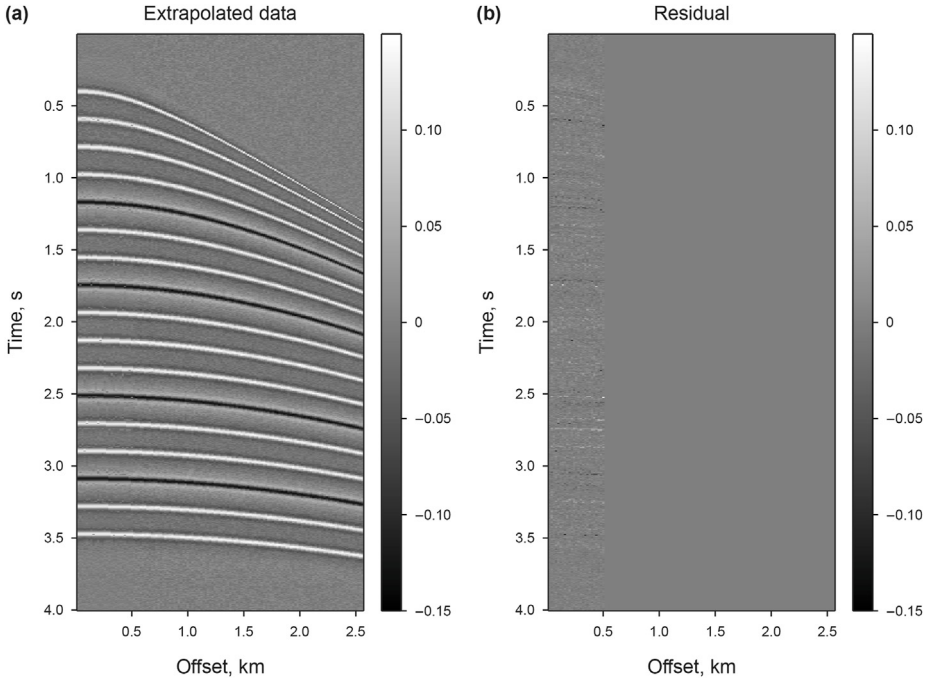

Fig. 20. **(a)** Extrapolated data using the proposed workflow (SNR = 4), **(b)** the residual between the extrapolated data and noisy data with a SNR of 4.

performance. Using the proposed workflow to process strong noise data with a SNR of 2, the TWT-warping profile and data reconstruction result are shown in Figs. 23 and 24, respectively. It can be seen that the method demonstrates good stability. The amplitude reconstruction error of this data is 47.94%, which is a significant reduction. It is worth mentioning that the amplitude average relative error values of the noisy data are all relatively large due to the unpredictability of random noise during the extrapolation process. However, the good performance of the proposed workflow can also be seen from the residual profile.

4. Field data application

The synthetic data above has verified the feasibility of the proposed workflow, and the comparison with previous method demonstrates its superiority. Next, we will demonstrate the applicability of the method using an ocean CMP gather released by Mobil Oil Company in 2002, as shown in Fig. 25(a). The time sampling rate is 4ms, and the spatial sampling rate is 0.05 km. Fig. 25(b) shows the field data after muted 20% near-offset seismic traces. The TWT-warping profile of missing data calculated in the

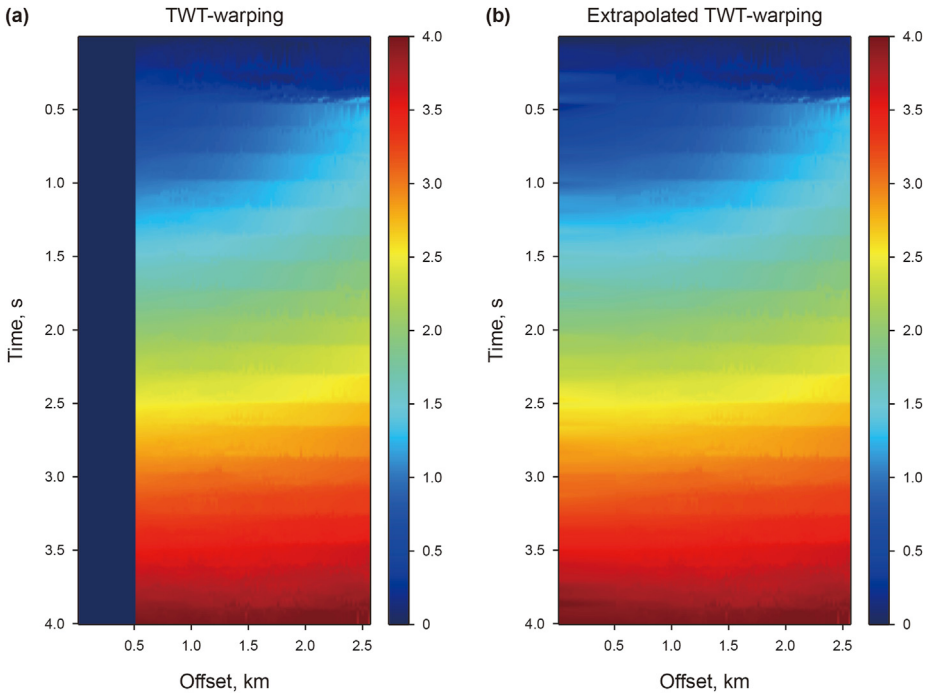

Fig. 21. **(a)** TWT-warping profile of noisy data with a SNR of 2 obtained through predictive painting, **(b)** extrapolated TWT-warping profile.

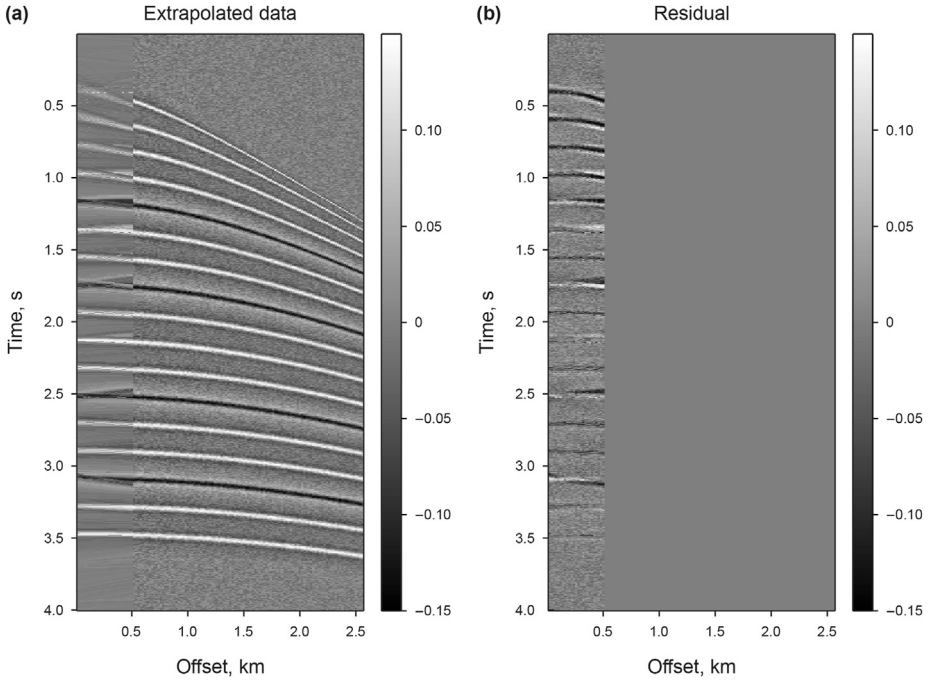

Fig. 22. **(a)** Extrapolated data through Khoshnavaz (2022) method (SNR = 2), **(b)** the residual between the extrapolated data and noisy data with a SNR of 2.

Khoshnavaz (2022) method is shown in Fig. 26(a). The extrapolation result of the TWT-warping profile is shown in Fig. 26(b), and the continuity of the shallow TWT is very poor. After further predicting the amplitude information, extrapolated data can be obtained, as shown in Fig. 27(a). Shallow data cannot be predicted accurately. Fig. 27(b) shows the difference profile between Figs. 25(a) and 27(a), and it can be seen that the seismic events are very obvious. To quantify the accuracy of the result, we calculated the relative error of the amplitude residual of the missing seismic traces relative to the original amplitude of the region, which is 60.84%, and the error is very large. Fig. 28(a) and (b) show the time-shift and TWT-warping profiles calculated using the MS-DTW method, respectively. Among them, we used five semicircle SE for this data processing. We used autoregressive polynomials to fit the TWT-warping profile, and then extrapolated data based on the fitted polynomial coefficients. The result is shown in Fig. 28(c).

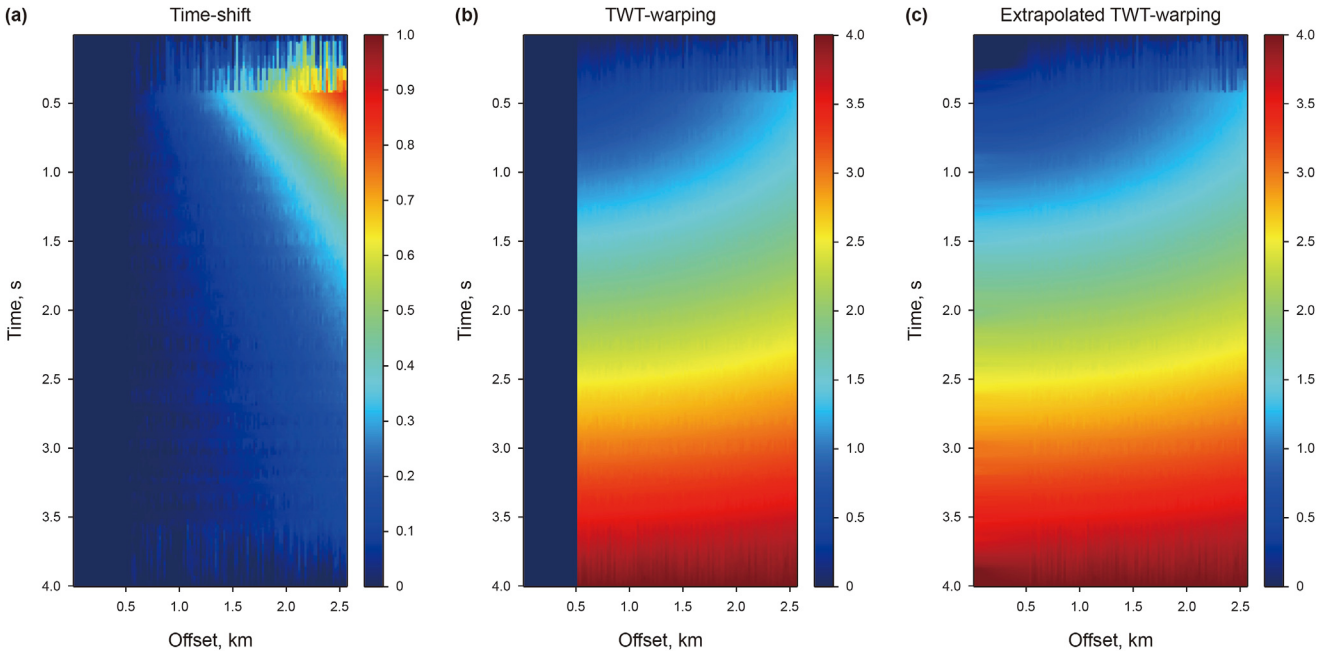

Fig. 23. **(a)** Time-shift of noisy data with SNR 2 calculated by MS-DTW, **(b)** TWT-warping profile calculated based on time-shift, **(c)** extrapolated TWT-warping profile.

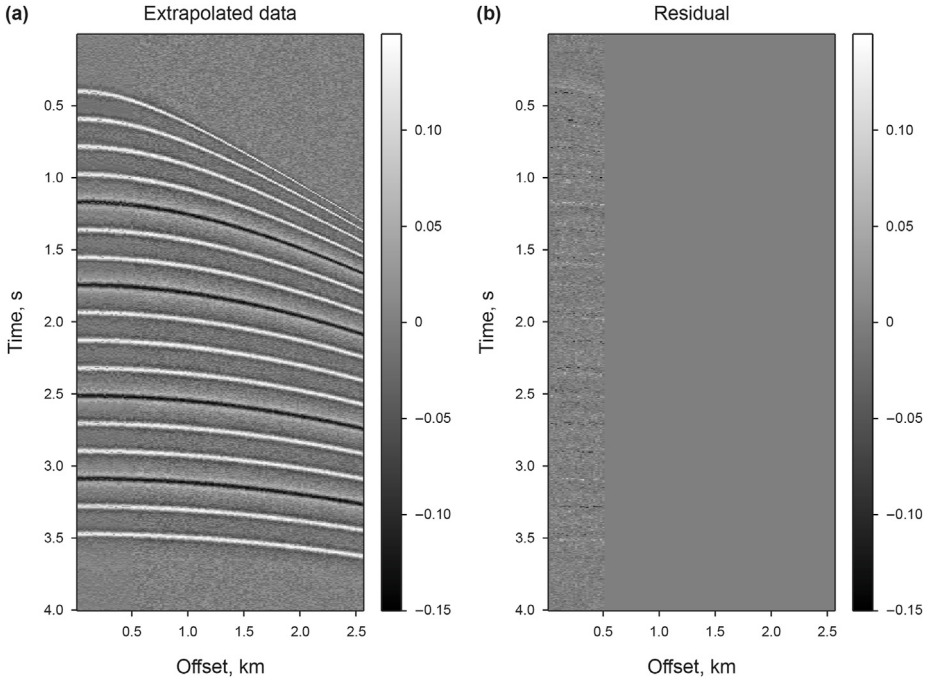

Fig. 24. **(a)** Extrapolated data using the proposed workflow (SNR = 2), **(b)** the residual between the extrapolated data and noisy data with a SNR of 2.

Further extract the amplitude based on TWT, and obtain the amplitude trend by fitting the weighted amplitude again. The final extrapolated data is shown in Fig. 29(a). Similarly, we demonstrate the amplitude energy difference between the extrapolated data and the original data, as shown in Fig. 29(b). We also calculated the average relative error of the reconstructed amplitude, which is approximately 31.39%. Compared with previous method, this error has been significantly reduced, and the result is also quite acceptable for field data, demonstrating the applicability of the proposed workflow.

5. Discussion

When implementing the proposed workflow, no assumptions are made regarding underground structures, indicating that our method is applicable to both isotropic and anisotropic media. To verify this conclusion, we tested the method using an anisotropic gather. Taking vertical transverse isotropic (VTI) media as an example, ray tracing is used to obtain traveltime information and inverse NMO is performed to generate an anisotropic gather, as shown in Fig. 30(a). The amplitude difference between it and the

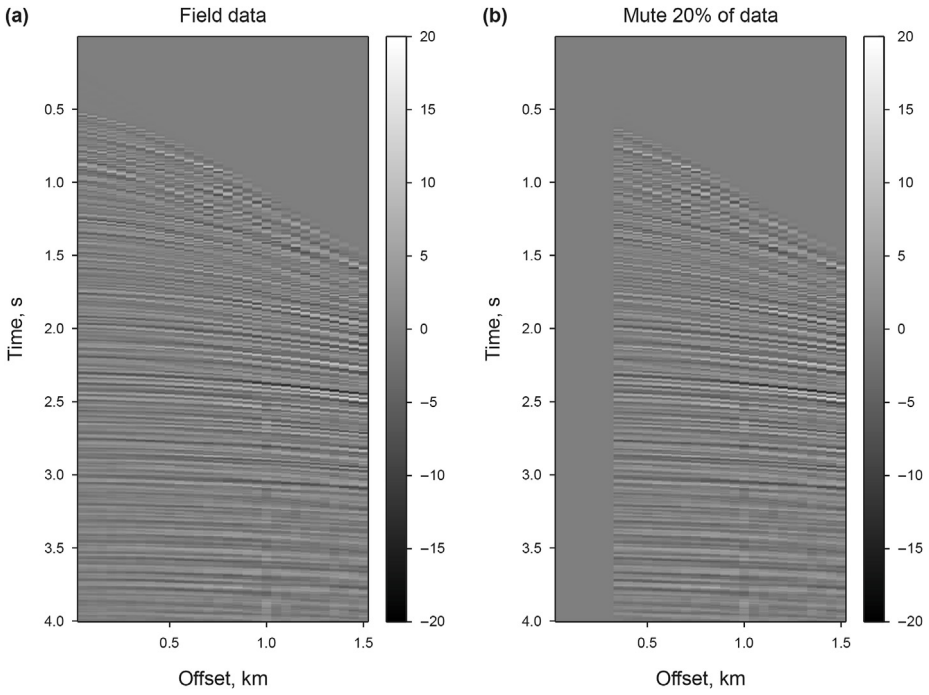

Fig. 25. **(a)** Field data released by Mobil Oil Company in 2002, **(b)** field data after muted 20%.

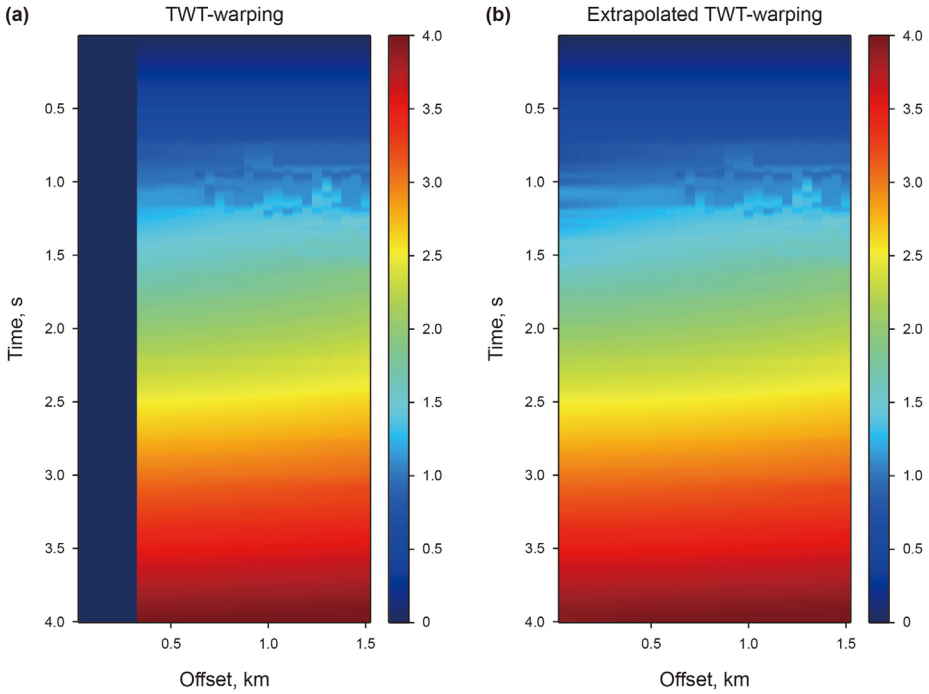

Fig. 26. **(a)** TWT-warping profile obtained through predictive painting, **(b)** extrapolated TWT-warping profile.

isotropic gather in Fig. 11(a) is shown in Fig. 30(b). Fig. 30(c) shows the anisotropic data with 20% near-offset data muted. The time-shift, TWT-warping profile, and extrapolated TWT-warping profile calculated using the proposed workflow are shown in Fig. 31(a)–(c), respectively. The reconstructed gather based on TWT is shown in Fig. 32(a), and it can be seen that the near-offset seismic traces have been well restored. Fig. 32(b) shows the residual between the reconstructed gather and the original anisotropic gather. We also calculated the relative error of amplitude residual relative to the amplitude of the original region, which is 2.7%. This result is ideal and proves the applicability of the proposed workflow to anisotropic media.

This workflow also has certain limitations. Due to the monotonicity principle that the DTW algorithm requires sequential matching between points during execution, our method is not suitable for data with cross events. In this paper, it is assumed that

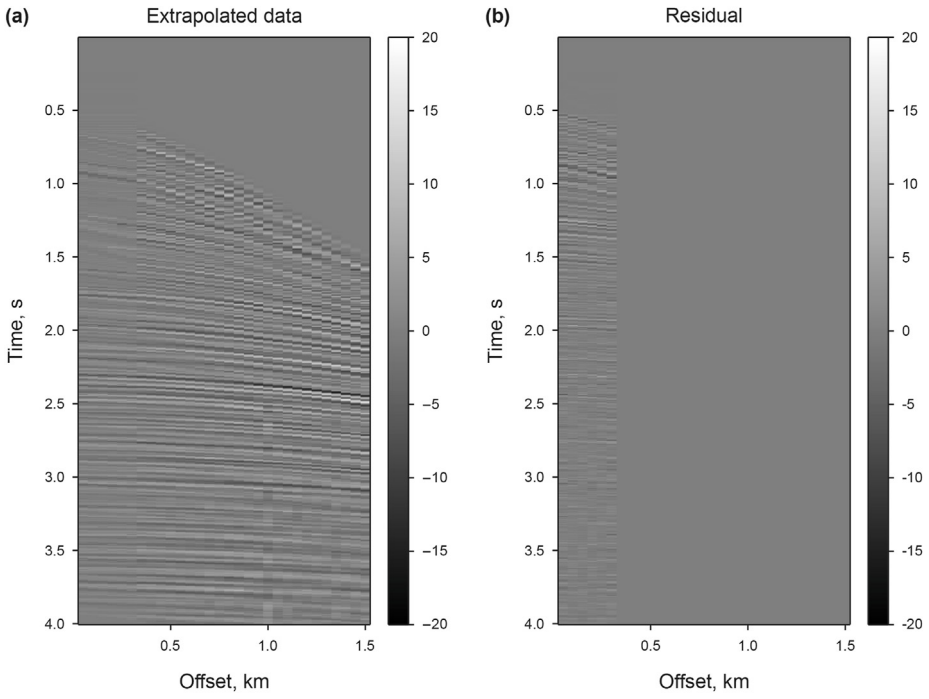

Fig. 27. **(a)** Extrapolated data using Khoshnavaz (2022) method, **(b)** the residual between the extrapolated data and the field data.

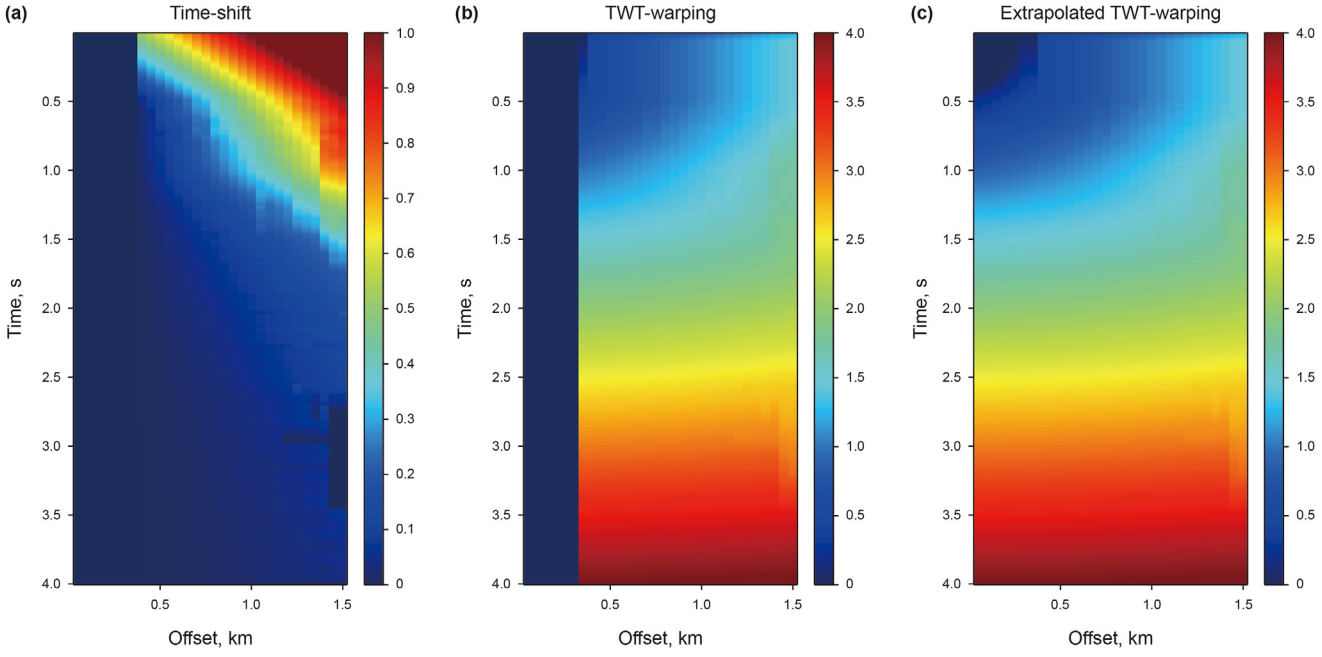

Fig. 28. **(a)** time-shift of missing data calculated by MS-DTW, **(b)** TWT-warping profile calculated based on time-shift, **(c)** extrapolated TWT-warping profile.

there are no cross events in the pre-stack gather being processed. In practical applications, this limitation can be solved by ignoring very far-offset data in the gather, as there may be cross events in the very far-offset data.

6. Conclusions

Irregularities are inevitable in the process of seismic data collection, which can affect subsequent processing. A new seismic data extrapolation workflow is proposed for reconstructing missing near-offset seismic traces in CMP gather. Firstly, a reference trace is selected and the time-shift between other traces and the reference trace is calculated using the MS-DTW. Time-shift is used as the basic input for this workflow and the TWT of each seismic trace is predicted from the time-shift. Autoregressive polynomial is fitted to the TWT for each seismic trace and the TWT curve is extrapolated from the polynomial coefficient. For a certain seismic event, the time window is determined based on its TWT curve, and the amplitudes within the time window are weighted and summed. Then, the amplitude information is fitted again with polynomials,

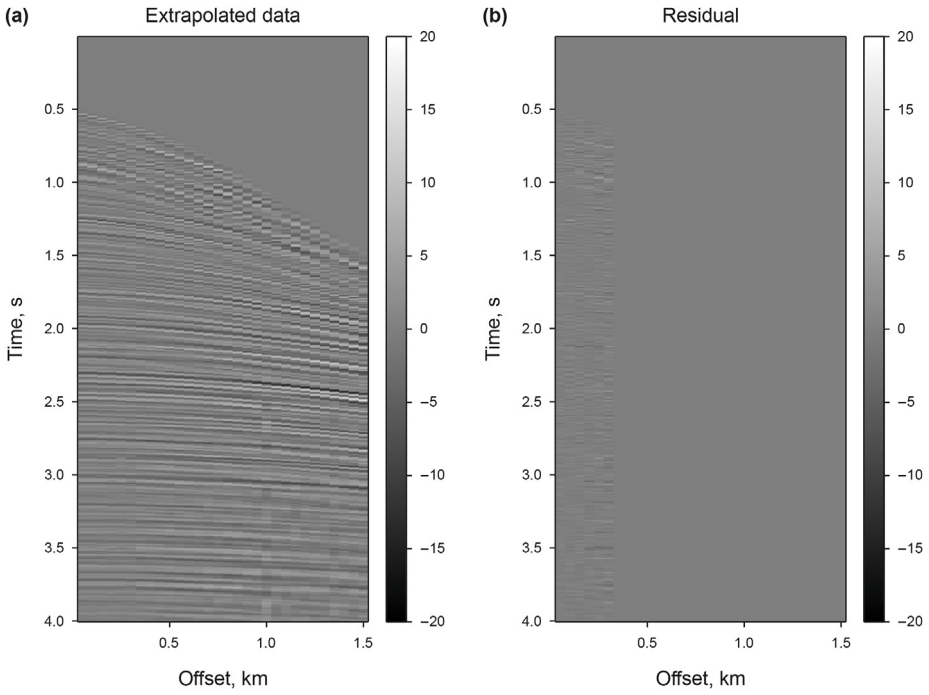

Fig. 29. **(a)** Extrapolated data using the proposed workflow, **(b)** the residual between the extrapolated data and the field data.

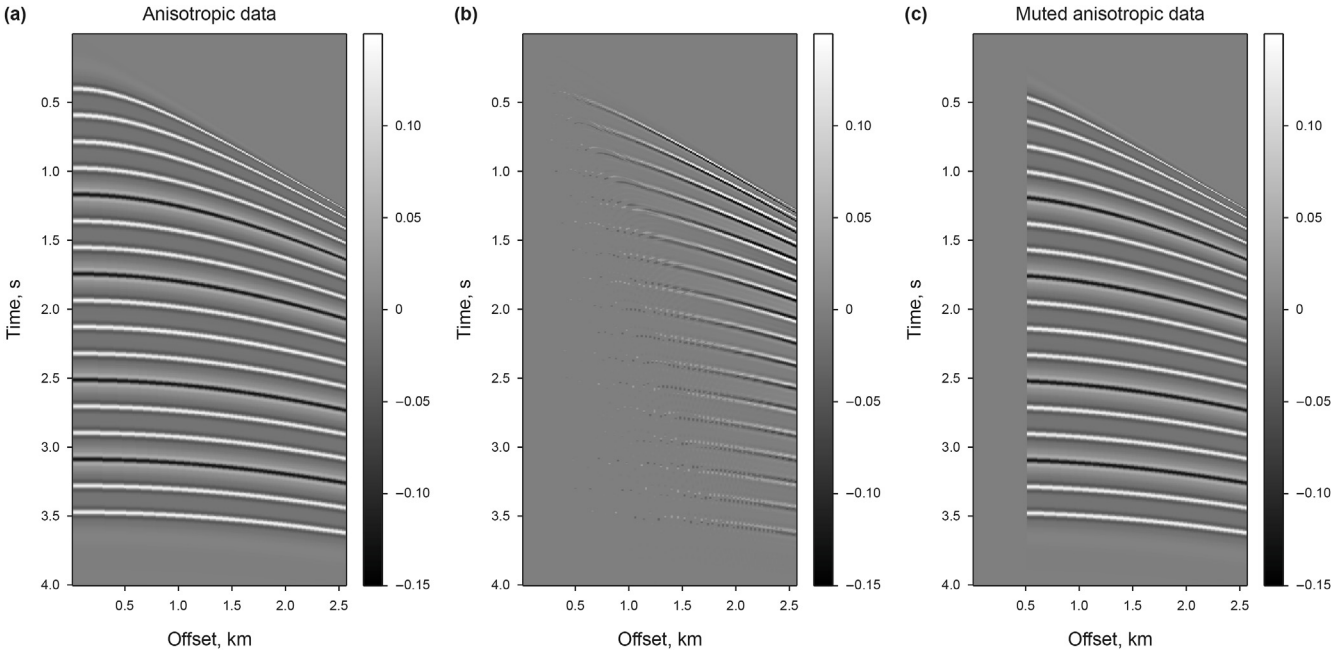

Fig. 30. **(a)** Anisotropic data, **(b)** the amplitude difference between anisotropic data and isotropic data, **(c)** anisotropic data with 20% near-offset seismic traces muted.

and the amplitude is extrapolated based on the obtained polynomial coefficients. Finally, an extrapolation workflow is completed. This workflow is based on the $t - x$ domain and does not require data conversion to other domains. Meanwhile, this workflow does not require any prior information about underground structures or velocity. We tested the workflow using synthetic data and the results showed that the proposed method can provide more accurate reconstruction results in the presence of strong noise compared to the method of predictive painting based on local slope. The application in field data has proven the applicability of the method.

CRediT authorship contribution statement

Jie-Li Li: Writing – original draft, Visualization, Validation, Software, Methodology, Investigation, Formal analysis, Conceptualization. **Wei-Lin Huang:** Writing – review & editing, Supervision, Resources, Project administration, Funding acquisition. **Rui-Xiang Zhang:** Writing – original draft.

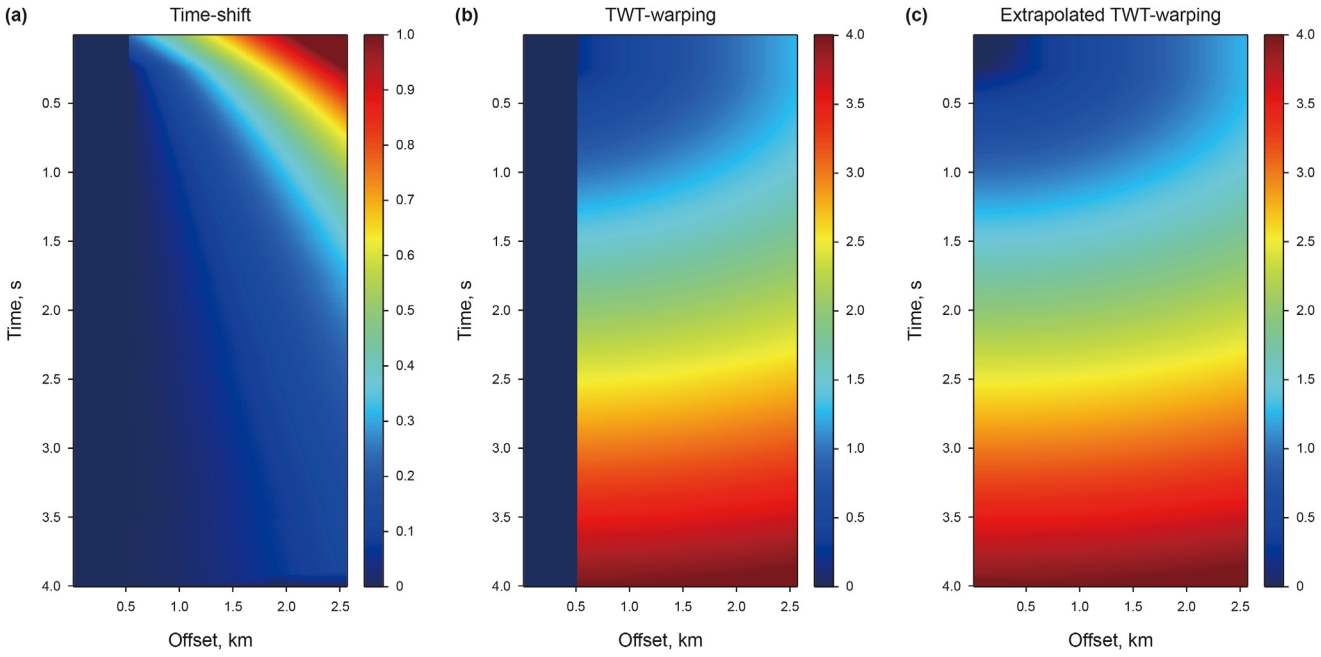

Fig. 31. (**a**) Time-shift of muted anisotropic data calculated by MS-DTW, (**b**) TWT-warping profile calculated based on time-shift, (**c**) extrapolated TWT-warping profile.

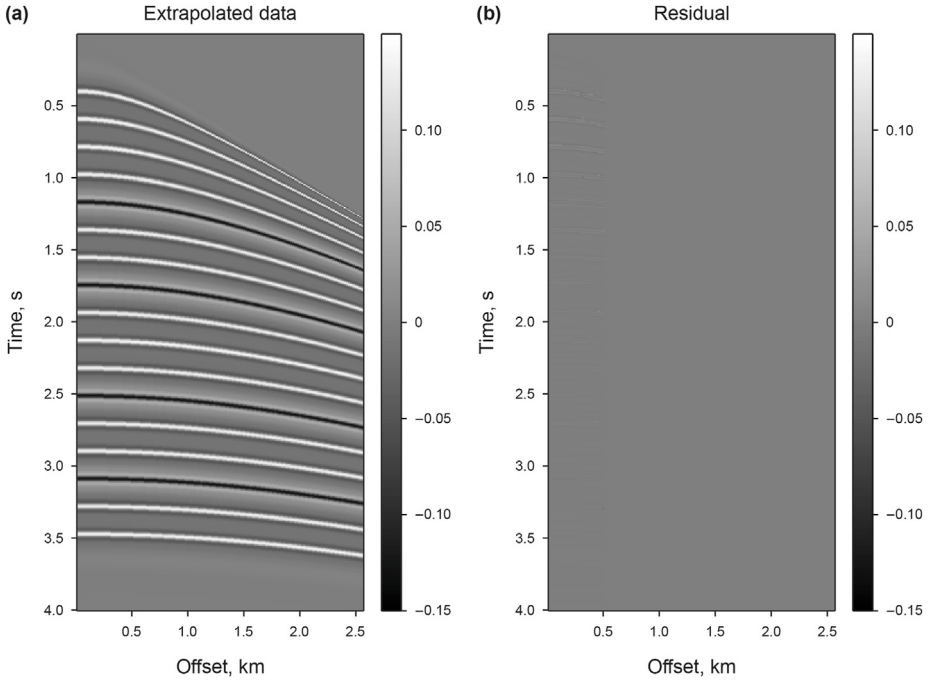

Fig. 32. (**a**) Extrapolated anisotropic data using the proposed workflow, (**b**) the residual between the extrapolated anisotropic data and original anisotropic data.

Declaration of competing interest

The authors declare the following financial interests/personal relationships which may be considered as potential competing interests:

Wei-Lin Huang is an editorial board member for Petroleum Science and was not involved in the editorial review or the decision to publish this article. All authors declare that there are no competing interests. If there are other authors, they declare that they have no known competing financial interests or personal relationships that could have appeared to influence the work reported in this paper.

Acknowledgement

We would like to express our gratitude to the sponsorship of the National Natural Science Foundation of China (42374133) and the Beijing Nova Program (2022056) for their funding of this research.

References

Alwon, S., 2018. Generative adversarial networks in seismic data processing. SEG Technical Program Expanded Abstracts, pp. 1991–1995. https://doi.org/10.1190/segam2018-2996002.1.

Bai, L.S., Liu, Y.K., Lu, H.Y., et al., 2014. Curvelet-domain joint iterative seismic data reconstruction based on compressed sensing. Chin. J. Geophys. 57 (9), 2937–2945. https://doi.org/10.6038/cjg20140919 (in Chinese).

Cao, J.J., Xu, C.H., Zhu, Y.F., 2023. Simultaneous reconstruction and denoising of seismic data using multi-channel singular spectrum analysis based on hierarchical clustering. Oil Geophys. Prospect. 58 (4), 818–829. https://doi.org/10.13810/j.cnki.issn.1000-7210.2023.04.007 (in Chinese).

Chai, X.T., Tang, G.Y., Wang, S.X., et al., 2021. Deep learning for irregularly and regularly missing 3-D data reconstruction. IEEE Trans. Geosci. Rem. Sens. 59 (7), 6244–6256. https://doi.org/10.1109/TGRS.2020.3016343.

Chemingui, N., 1996. Handling the irregular geometry in wide-azimuth surveys. SEG Tech. Progr. Expand. Abstr. 15 (1), 2106. https://doi.org/10.1190/1.1442366.

Chen, S.Q., Jin, S., Li, X., et al., 2018. Nonstretching normal-moveout correction using a dynamic time warping algorithm. Geophysical 83 (1), V27–V37. https://doi.org/10.1190/geo2016-0673.1.

Chen, Y., Yu, S.W., Ma, J.W., 2023. A projection-onto-convex-sets network for 3D seismic data interpolation. Geophysics 88 (3), 249–265. https://doi.org/10.1190/geo2022-0326.1.

Cheng, J.K., Sacchi, M., Gao, J.J., 2019. Computational efficient multidimensional singular spectrum analysis for prestack seismic data reconstruction. Geophysics 84 (2), V111–V119. https://doi.org/10.1190/geo2018-0343.1.

Creswell, A., White, T., Dumoulin, V., et al., 2018. Generative adversarial networks: an overview. IEEE Signal Process. Mag. 35 (1), 53–65. https://doi.org/10.1109/MSP.2017.2765202.

Fang, W., Fu, L., Liu, S., et al., 2021. De-aliased seismic data interpolation using a deep learning-based prediction-error filter. Geophysics 86 (4), V317–V328. https://doi.org/10.1190/geo2020-0487.1.

Fomel, S., 2002. Applications of plane-wave destruction filters. Geophysics 67 (6), 1946–1960. https://doi.org/10.1190/1.1527095.

Fomel, S., 2010. Predictive painting of 3D seismic volumes. Geophysics 75 (4), A25–A30. https://doi.org/10.1190/1.3453847.

Hale, D., 2013. Dynamic warping of seismic images. Geophysics 78 (2), S105–S115. https://doi.org/10.1190/geo2012-0327.1.

He, T., Wu, B.Y., Zhu, X., 2021. Seismic data consecutively missing trace interpolation based on multistage neural network training process. Geosci. Rem. Sens. Lett. IEEE 19, 7504105. https://doi.org/10.1109/LGRS.2021.3089585.

Hou, X.W., Tong, S.Y., Wang, Z.C., et al., 2023. Sparse seismic data reconstruction based on a convolutional neural network algorithm. J. Ocean Univ. China 22 (2), 410–418. https://doi.org/10.1007/s11802-023-5138-z (in Chinese).

Huang, W.L., Wang, R.Q., Chen, Y.K., 2018. Regularized non-stationary morphological reconstruction algorithm for weak signal detection in microseismic monitoring: methodology. Geophys. J. Int. 213, 1189–1211. https://doi.org/10.1093/gji/ggy054.

Huang, W.L., Feng, D.S., Chen, Y.K., 2020. De-aliased and de-noise Cadzow filtering for seismic data reconstruction. Geophys. Prospect. 68 (2), 553–571. https://doi.org/10.1111/1365-2478.12867.

Huang, W.L., Liu, J.X., 2020. Robust seismic image interpolation with mathematical morphological constraint. IEEE Trans. Image Process. 29, 819–829. https://doi.org/10.1109/TIP.2019.2936744.

Huang, W.L., 2022. Seismic data interpolation by Shannon Entropy-based shaping. IEEE Trans. Geosci. Rem. Sens. 60, 1–12. https://doi.org/10.1109/TGRS.2022.3180200.

Huang, W.L., 2023. A genetic algorithm optimized undersampling method for seismic sparse acquisition and reconstruction. IEEE Trans. Geosci. Rem. Sens. 61, 1–10. https://doi.org/10.1109/TGRS.2023.3252277.

Huangfu, M.M., 2021. Reconsitution of Irregular Seismic Data Based on Recurrent Neural Network. Harbin Institute of Technology. https://doi.org/10.27061/d.cnki.ghgdu.2021.001975. Master's thesis (in Chinese).

Khoshnavaz, M.J., Siahkoohi, H.R., Bona, A., 2018. Attenuation of spatial aliasing in CMP domain by non-linear interpolation of seismic data along local slopes. J. Earth Space Phys. 44 (4), 73–85. https://doi.org/10.22059/JESPHYS.2018.257443.1007005.

Khoshnavaz, M.J., 2022. Oriented extrapolation of common-midpoint gathers in the absence of near-offset data using predictive painting. Geophys. Prospect. 70, 725–736. https://doi.org/10.1111/1365-2478.13195.

Kumar, U., Legendre, C.P., Li, Z., et al., 2022. Dynamic time warping as an alternative to windowed cross correlation in seismological applications. Seismol Res. Lett. 93 (3), 1909–1921. https://doi.org/10.1785/0220210288.

Lan, N.Y., Zhang, F.C., Yin, X.Y., 2022. Seismic data reconstruction based on low dimensional manifold model. Petrol. Sci. 19 (2), 518–533. https://doi.org/10.1016/j.petsci.2021.10.014.

Li, J.L., Liu, G.C., 2021. Automatic horizon extraction method of seismic data based on plane wave similarity. In: 82nd EAGE Annual Conference & Exhibition, pp. 1–5. https://doi.org/10.3997/2214-4609.202010920.

Li, J.L., Liu, G.C., Zhang, R.X., 2021. Automatic extraction of horizons through faults. In: 82nd EAGE Annual Conference & Exhibition, pp. 1–5. https://doi.org/10.3997/2214-4609.202113115.

Li, J.L., Huang, W.L., 2022. Automatic extraction of seismic data horizon across faults. IEEE Trans. Geosci. Rem. Sens. 60, 1–11. https://doi.org/10.1109/TGRS.2022.3169912.

Li, Z.C., Qu, Y.M., 2022. Research progress on seismic imaging technology. Petrol. Sci. 19 (1), 128–146. https://doi.org/10.1016/j.petsci.2022.01.015.

Li, X.L., Wei, Y.J., Ouyang, W., et al., 2023a. Multi-parameter non-iterative linearized inversion using angle-domain generalized Radon transform. Chin. J. Geophys. 66 (1), 383–400. https://doi.org/10.6038/cjg2022P0676 (in Chinese).

Li, P.Y., Zhang, Y.L., Li, Z., et al., 2023b. Iterative shrinkage-thresholding algorithm with inertia and dry friction for convolutional dictionary learning. Digit. Signal Process. 140. https://doi.org/10.1016/j.dsp.2023.104139.

Li, J.L., Huang, W.L., Zhang, R.X., 2023c. Velocity-independent NMO correction based on multi-scale dynamic time warping. In: 84th EAGE Annual Conference & Exhibition, pp. 1–5. https://doi.org/10.3997/2214-4609.2023101448.

Liu, D.J., Huang, J.P., Wang, Z.Y., 2020. Convolution-based multi-scale envelope inversion. Petrol. Sci. 17 (2), 352–362. https://doi.org/10.1007/s12182-019-00419-8.

Liu, L., Fu, L.H., Zhang, M., 2021. Deep-seismic-prior-based reconstruction of seismic data using convolutional neural networks. Geophysics 86 (2), V131–V142. https://doi.org/10.1190/geo2019-0570.1.

Liu, N.H., Zhang, B., Gao, J.H., et al., 2018. Seismic attenuation estimation using the modified log spectral ratio method. J. Appl. Geophys. 159, 386–394. https://doi.org/10.1016/j.jappgeo.2018.09.014.

Liu, N.H., Zhang, B., Gao, J.H., et al., 2019. Seismic anelastic attenuation estimation using prestack seismic gathers. Geophysics 84 (6), M37–M49. https://doi.org/10.1190/geo2017-0811.1.

Liu, N.H., Wu, L.K., Wang, J.L., et al., 2022a. Seismic data reconstruction via wavelet-based residual deep learning. IEEE Trans. Geosci. Rem. Sens. 60. https://doi.org/10.1109/TGRS.2022.3152984.

Liu, Y., Wu, G., Zheng, Z., 2022b. Seismic data interpolation without iteration using a txy streaming prediction filter with varying smoothness. Geophysics 87 (1), V29–V38. https://doi.org/10.1190/geo2021-0052.1.

Luke, D., Zhang, Q.S., 2019. Quantifying and correcting residual azimuthal anisotropic moveout in image gathers using dynamic time warping. Geophysics 85 (5), O71–O82. https://doi.org/10.1190/geo2019-0324.1.

Oboué, Y.A.S.I., Chen, Y.K., 2021. Mixed rank-constrained model for simultaneous denoising and reconstruction of 5-D seismic data. IEEE Trans. Geosci. Rem. Sens. 60, 1–13. https://doi.org/10.1109/TGRS.2021.3072056.

Oikawa, K., Saito, H., Kuroda, S., et al., 2021. Comparing two interpolation methods based on POCS for determining EM wave velocity from sparse CMP data. Proceedings of the 14th SEGJ International Symposium 146–149. https://doi.org/10.1190/segj2021.

Orchard, G., Zhang, J., Suo, Y., et al., 2012. Real time compressive sensing video reconstruction in hardware. IEEE Journal on Emerging & Selected Topics in Circuits & Systems 2 (3), 604–615. https://doi.org/10.1109/JETCAS.2012.2214614.

Park, M.J., Jennings, J., Clapp, B., et al., 2020. Seismic data interpolation using a POCS-guided deep image prior. 90th Annual International Meeting, SEG Expanded Abstracts 3154–3158. https://doi.org/10.1190/segam2020-3427320.1.

Ronen, J., 1987. Wave-equation trace interpolation. Geophysics 52 (7), 973–984. https://doi.org/10.1190/1.1442366.

Shang, G.J., Huang, W.L., Yuan, L.K., et al., 2022. Automatic microseismic events detection using morphological multiscale top-hat transformation. Petrol. Sci. 19 (5), 2027–2045. https://doi.org/10.1109/TGRS.2019.2953676.

Smith, T., Waterman, M., 1980. New stratigraphic correlation techniques. J. Geol. 88, 451–457. https://doi.org/10.1086/628528.

Sobania, A., Evans, J.P.O., 2005. Morphological corner detector using paired triangular structuring elements. Pattern Recogn. 38 (7), 1087–1098. https://doi.org/10.1016/j.patcog.2004.10.009.

Song, H., Gao, Y., Chen, W., et al., 2020. Seismic data denoising based on convolutional autoencoder denoising. Oil Geophys. Prospect. 55 (6), 1210–1219. https://doi.org/10.13810/j.cnki.issn.1000-7210.2020.06.006 (in Chinese).

Spitz, S., 1991. Seismic trace interpolation in the F-X domain. Geophysics 56 (6), 785–794. https://doi.org/10.1190/1.1443096.

Sun, H.M., Jia, R.S., Zhang, X.L., et al., 2019. Reconstruction of missing seismic traces based on sparse dictionary learning and the optimization of measurement matrices. J. Petrol. Sci. Eng. 175, 719–727. https://doi.org/10.1016/j.petrol.2019.01.016.

Tang, H.H., Mao, W.J., Zhan, Y., 2020. Reconstruction of 3D irregular seismic data with amplitude preserved by high-order parabolic Radon transform. Chin. J. Geophys. 63 (9), 3452–3464. https://doi.org/10.6038/cjg2020N0053 (in Chinese).

Venstad, J.M., 2014. Dynamic time warping an improved method for 4D and tomography time shift estimation. Geophysics 79 (5), R209–R220. https://doi.org/10.1190/geo2013-0239.1.

Vintsyuk, T.K., 1968. Speech discrimination by dynamic programming. Cybern. Syst. Anal. 4, 52–57. https://doi.org/10.1007/BF0107475.

Wang, R.Q., Zheng, G.J., Fu, H.Z., et al., 2005. Noise-eliminated method by morphologic filtering in seismic data processing. Oil Geophys. Prospect. 40 (3), 277–282 (in Chinese).

Wang, H., Yan, J.Y., Fu, G.M., et al., 2020. Current status and application prospect of deep learning in geophysics. Prog. Geophys. 35 (2), 642–655. https://doi.org/10.6038/pg2020CC0476 (in Chinese).

Yi, J.D., Zhang, M., Li, Z.C., et al., 2023. Review of deep learning seismic data reconstruction methods. Prog. Geophys. 38 (1), 361–381. https://doi.org/10.6038/pg2023GG0048 (in Chinese).

Yoon, D., Yeeh, Z., Byun, J., 2021. Seismic data reconstruction using deep

bidirectional long short-term memory with skip connections. Geosci. Rem. Sens. Lett. IEEE 18 (7), 1298–1302. https://doi.org/10.1109/LGRS.2020.2993847.
Yuan, C.C., Bryan, J., Denolle, M., 2021. Numerical comparisonof time-, frequency- and wavelet-domain methods for coda wave interferometry. Geophys. J. Int. 226 (2), 828–846. https://doi.org/10.1093/GJI/GGAB140.
Zhang, H., Wang, D.N., Li, H.X., et al., 2017. High accurate seismic data reconstruction based on non-uniform curvelet transform. Chin. J. Geophys. 60 (11), 4480–4490. https://doi.org/10.6038/cjg20171132 (in Chinese).
Zhang, L., Liu, C., Hu, B., et al., 2021. Reconstruction of regolith structure from lunar penetrating radar channel 2 data based onshearlet transform. Chin. J. Geophys. 64 (8), 2888–2899. https://doi.org/10.6038/cijg202100350 (in Chinese).
Zheng, Z.Y., Dai, W.R., Xue, D.D., et al., 2023. Hybrid ISTA: unfolding ISTA with convergence guarantees using free-form deep neural networks. IEEE Trans. Pattern Anal. Mach. Intell. 45 (3), 3226–3244. https://doi.org/10.1109/TPAMI.2022.3172214.
Zhou, L., Liao, J.P., Liu, X.Y., et al., 2023. A high resolution inversion method for fluid factor with dynamic dry rock VP/VS ratio squared. Petrol. Sci. 20 (5), 2822–2834. https://doi.org/10.1016/j.petsci.2023.09.015.
Zhou, S.W., Zhang, D.X., 2023. Adsorbed and free gas occurrence characteristics and controlling factors of deep shales in the southern Sichuan Basin, China. Petrol. Sci. 20 (3), 1301–1311. https://doi.org/10.1016/j.petsci.2022.12.006.